Increasing Sensitivity to Soil Moisture Deficits Predominantly Intensifies Evapotranspiration Stress in a Greening China

Yuan Liu[1], Yong Wang[1,2], Yong Zhao[1,2], Shouzhi Chen[3], Longhao Wang[4,5], Wenjing Yang[6], Xing Li[1], Xinxi Li[7], Huimin Lei[8], Huanyu Chang[9], Jiaqi Zhai[1,2], Yongnan Zhu[1,2], Qingming Wang[1,2], and Ting Ye[10]

5

[1]State Key Laboratory of Simulation and Regulation of Water Cycle in River Basin, China Institute of Water Resources and Hydropower Research (IWHR), Beijing, 100038, China
[2]Key Laboratory of Water Safety for Beijing-Tianjin-Hebei Region of Ministry of Water Resources, China Institute of Water Resources and Hydropower Research (IWHR), Beijing, 100038, China
10   [3]College of Water Sciences, Beijing Normal University, Beijing, 100875, China
[4]Key Laboratory of Water Cycle and Related Land Surface Processes, Chinese Academy of Sciences, Beijing, 100101, China
[5]Institute of Geographic Sciences and Natural Resources Research, University of Chinese Academy of Sciences, Beijing, 100049, China
15   [6]National Centre for Groundwater Research and Training, Flinders University, Adelaide, SA 5001, Australia
[7]PowerChina Asia & Pacific, Power Construction Corporation of China, Beijing, 100038, China
[8]State Key Laboratory of Hydroscience and Engineering, Department of Hydraulic Engineering, Tsinghua University, Beijing, 100084, China
[9]Academy of Eco-civilization Development for Jing-Jin-Ji Megalopolis, Tianjin Normal University, Tianjin, 300387, China
20   [10]State Key Laboratory of Water Resources and Hydropower Engineering Science, Wuhan University, Wuhan, 430072, China

Correspondence to: Yong Wang (wangyong@iwhr.com)

Abstract. Amidst drastic environmental changes, the intricate interplay and feedback mechanisms in the water-vegetation-atmosphere nexus experience alteration. Previous research primarily centers on the responses among variables within this

25   system, with little known about whether and how these responses (sensitivities) change. Here, we employ the Evapotranspiration Stress Index (ESI) to represent the equilibrium of the nexus and develop a memory dynamic linear model based on Bayesian forward filtering. The model takes into account the carry-over effect in the "dry gets drier" self-amplify loop, allowing for a more effective estimation of the ESI time-varying sensitivity to associated influencing factors. To corroborate the model, a 5-year moving window multiple linear regression is applied to estimate the approximate sensitivity

30   fluctuations. Our analysis reveals that from 1950 to 2020, mainland China experienced a notable 4.74% escalation in evapotranspiration stress. This is primarily attributed to surface soil moisture, whose sensitivity to ESI surged by 1.25-fold in the last decade compared to the early 2000s. Vapor Pressure Deficit (VPD) and Leaf Area Index (LAI) also exerted a substantial role, with their sensitivities fluctuating approximately 0.95% and -0.56%, respectively. Moreover, the greening pace is linked to an increase in soil moisture sensitivity and a decrease in VPD sensitivity, suggesting that rapid greening

35   may alter the ecological resilience against soil deficit and atmospheric drought. Our findings underscore the spatiotemporal

variations in sensitivity, enriching the comprehension of ecosystem reactions to external factors, and offer essential insights for refining Earth System Model parameters and advancing greening endeavors.

Graphical Abstract
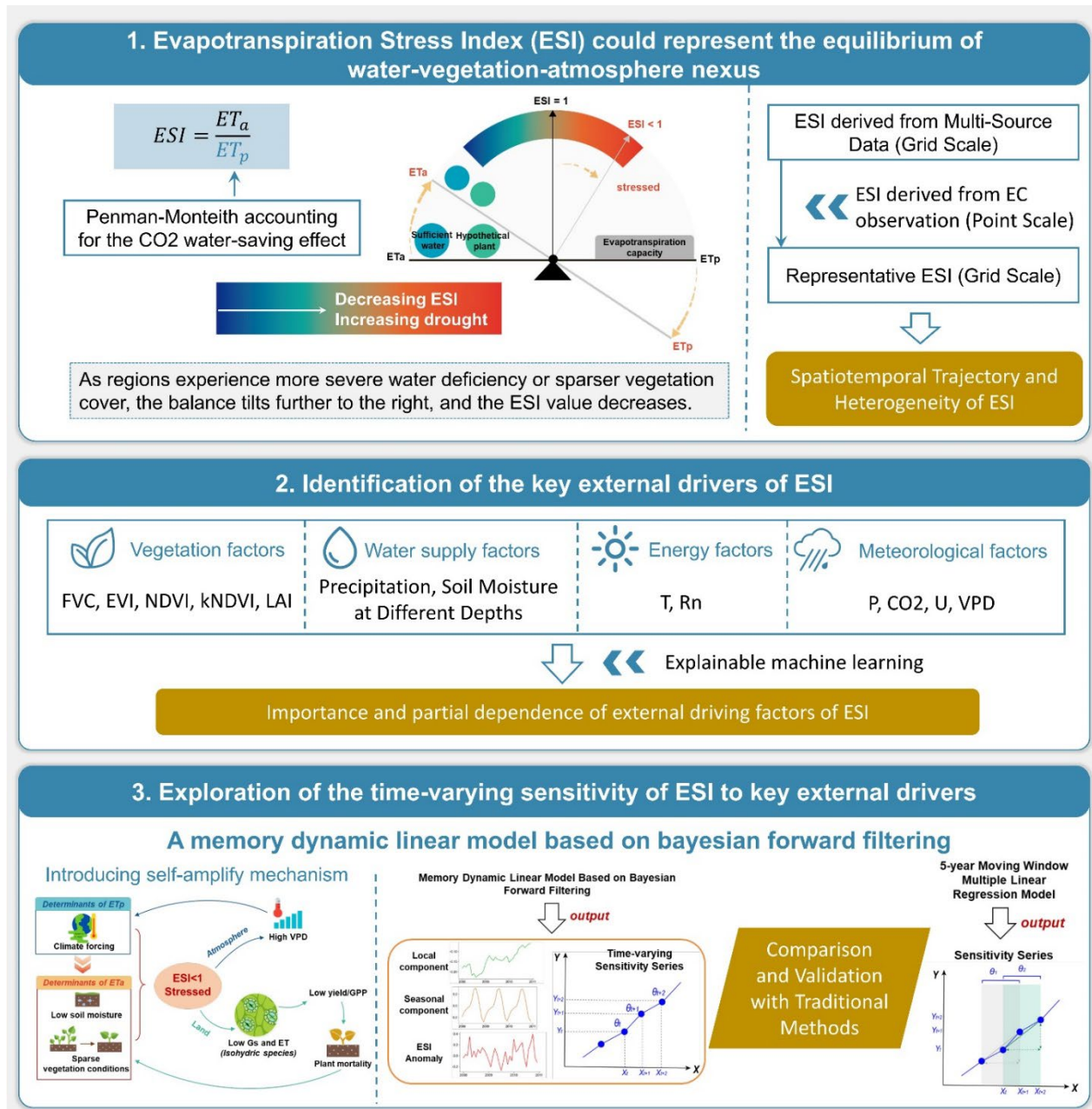
1 Introduction

Over the last two decades, approximately one-third of the global land has experienced vegetation greening(Chen et al., 2019). Concurrently, 53% to 64% of these regions have undergone atmospheric desiccation(Yuan et al., 2019). However, research has also revealed a rise in available water resources (precipitation supply minus evapotranspiration loss) in ~45% proximate and downwind zones(Cui et al., 2022). Contrary to greening, satellite-based studies have indicated a 0.4-fold expansion in regions shifting from greening to browning(De Jong et al., 2013; Liu et al., 2023). Amidst the ongoing debates over greening or browning, and wetting or drying, it is unequivocal that the intricate interactions and feedback mechanisms among water, vegetation, and climate are altered.

Defined as the ratio of actual to potential evapotranspiration, the Evapotranspirative Stress Index (ESI) can comprehensively reflect the equilibrium between water supply, vegetation status, and climatic conditions(Anderson et al., 2013, 2016) (Fig. 1ab). Potential evapotranspiration (ETp) represents the evaporation potential under ideal circumstances—ample water supply, uniform plant growth, and consistent crop coverage (specifically, alfalfa)—and generally considered to be influenced solely by climatic factors (Allen et al., 1998; Li et al., 2022b; Thornthwaite, 1948). Regions suffering from water scarcity or limited vegetation cover are subject to evapotranspirative stress (Fig. 1b), whereas ample water or vigorous vegetation may result in actual evapotranspiration surpassing the hypothetical potential (Liu et al., 2022) (Fig. 1a). This occurs because, during the calculation of ETp, parameters such as canopy reflectance coefficient and surface resistance are fixed for a hypothetical crop, whereas actual vegetation characteristics can exceed those assumptions. Previous research has proven the the high sensitivity of ESI to early-stage drought, as plant naturally curtails its water consumption before drought fully manifest (Nguyen et al., 2019; Otkin et al., 2018). Therefore, comprehending the underlying mechanisms and associated factors of ESI dynamics is crucial for implementing prompt and effective drought mitigation strategies, protecting stable ecosystems, and maintaining high yields.

The evolution of evapotranspiration (ET) stress includes a positive "dry gets dryer" land-atmosphere feedback (Fu et al., 2022; Gentine et al., 2019; Seneviratne et al., 2010) (Fig. 1c). Regions subjected to climate-induced ET stress are characterized by low soil moisture and weak vegetation vitality. Isohydric species, in response, will close their stomata to minimize water loss, albeit at the cost of decreased photosynthesis and diminished carbon accumulation (Grossiord et al., 2020; Joshi et al., 2022). On one side, this reduction in water vapor release into the atmosphere intensifies atmospheric dryness, further reinforcing climate constraints. On the other side, sustained stress may cause plant mortality due to hydraulic failure and carbon starvation, resulting in progressively sparser terrestrial vegetation coverage (Kono et al., 2019; Mantova et al., 2022). Such a self-amplify loop highlights the necessity to consider temporal connections or sustained effects when exploring the ET stress dynamics. Research based on data analysis and field experiments has uncovered that such internal memory effects are particularly pronounced in water-limited areas (Liu et al., 2018; Richard et al., 2008; Xiao et al., 2024a). Statistically, the autocorrelation component can serve as a good representation of internal memory effects (Forzieri et al., 2022; Smith et al., 2022). For example, Kusch et al., (2022)employed Normalized Difference Vegetation Index (NDVI)

lagged by one time step as a representation of intrinsic-vegetation memory and compared its role with external meteorological factors in resisting adverse environmental disturbance. Theoretically, an increase in the autocorrelation coefficient suggests a decline in ecosystem resilience to external interventions or an approach to critical thresholds (Liu, 2019; Scheffer et al., 2009).It is disappointing that existing research primarily concentrated on external driving factors, such as meteorological, hydrological, and biotic drivers (Feng et al., 2020; Fu et al., 2024b; Jung et al., 2010; Liu et al., 2020c; Peng et al., 2019).Therefore, integrating the co-regulation of external forcing factors with internal memory effects is essential for an in-depth investigation into the dynamics of ET stress and ecological responses.
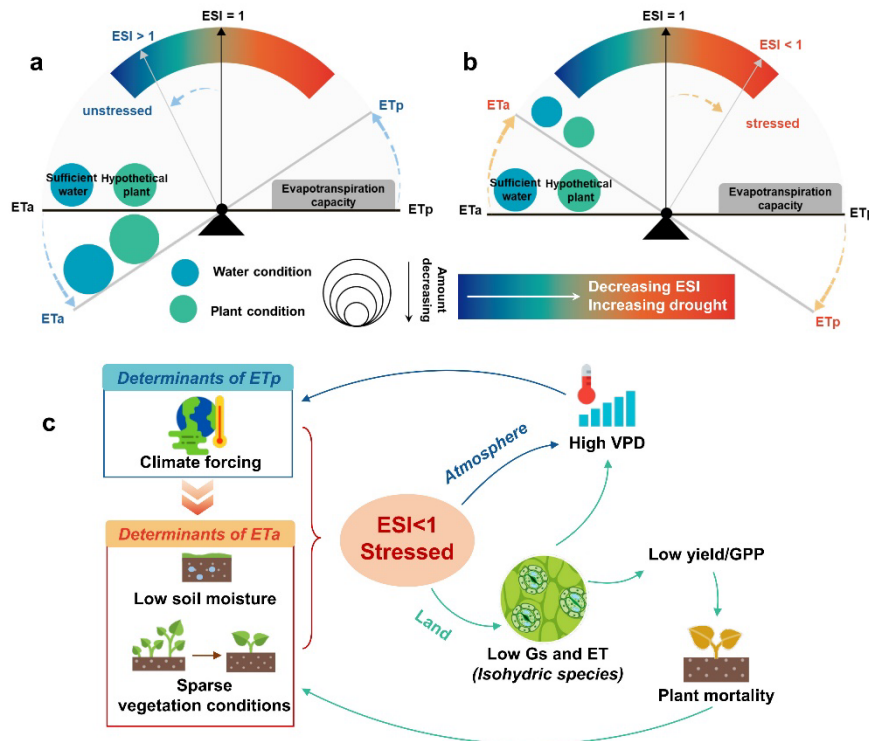
Figure 1. Conceptual diagram of evapotranspiration stress and its self-amplify loop. (a) ESI represents the hydrological-vegetation-atmosphere equilibrium, defined as the ratio of actual evapotranspiration (ETa) to potential evapotranspiration (ETp). When using the parameters of crops assumed in the PM equation to calculate ETp (also known as ET$_0$, reference crop evapotranspiration in agriculture), ESI values greater than 1 may occur. (b) As regions experience more severe water deficiency or sparser vegetation cover, the balance tilts further to the right, and the ESI value decreases. A smaller ESI value indicates more severe drought conditions. (c) Schematic of the self-amplify feedback loop, where Gs represents stomatal conductance, GPP stands for gross primary productivity, and VPD denotes vapor pressure deficit. Blue lines depict the atmospheric feedback pathway, while green lines represent the terrestrial surface process pathway.

Variations in regional evaporation stress patterns arise from different response to relevant factors. Soil moisture acts as the supply side of evaporation, while vapor pressure deficit (VPD), as the demand side, pulls water from soil pores and plant stomata into the atmosphere (Dong et al., 2020; Liu et al., 2020b). As an alleviator, increased ambient CO_2 can mitigate evaporation by enhancing water use efficiency (Li et al., 2023; Liu et al., 2017). Among these external drivers, mounting

evidence emphasizes the pronounced sensitivity to moisture and VPD (Liu et al., 2020a; Sulman et al., 2016; Zhang et al., 2021a; Zhong et al., 2023). However, several studies also argue that vegetation structure, characterized by the Leaf Area

95 Index (LAI), plays a key role in controlling the distribution of surface energy and land-atmosphere coupling that determines evapotranspiration (Fu et al., 2022). In addition to regional characteristic dependence, the differing sampling time spans are also important contributors to the inconsistent results. In an ever-changing world, the sensitivity of evaporation stress to environmental changes may also evolve (Hsu and Dirmeyer, 2023). However, research on the time-varying sensitivity is still in its infancy, even the state-of-the-art Earth System Models have not yet incorporated it into parameterization schemes.

100 Existing research investigates these temporal changes by segmenting time series. For instance, Zeng et al., (2022)conducted a regression analysis with 5-year moving window to derive the time series of sensitivity coefficients, which represent the NDVI's response to precipitation. Similarly, Li et al., (2022) applied interpretable machine learning algorithms to compute the sensitivity of LAI to soil water per 3-year-block data during 1982 to 2017 to investigate its temporal changes. However, these approaches only yield average response for each segment, rather than the true "instantaneous or dynamic" sensitivity.

105 Fortunately, the application of Dynamic Linear Model based on Bayesian forward filtering, as demonstrated by Zhang et al., (2022) in their recent research of global NDVI sensitivity to precipitation, offers a promising avenue to elucidate this problem.

Here, a memory dynamic linear model (MDLM) that considers both the intrinsic lagged effect and the concurrent extrinsic forcing has been developed to capture not only how ESI responds to a changing environment, but also how this response

110 varies. Utilizing the MDLM, we calculate the time-varying sensitivity of ESI to its influential factors at pixel scale in China over the past 20 years with an 8-day temporal granularity. The robutness of the results is verified through a moving-window multiple linear regression model. Before running these model, the interpretable machine learning algorithms based on two classifiers are employed to screen key drivers of ESI across diverse climate-vegetation zones on 8-, 16-, and monthly time scales. The overarching aim of this study is to (a) untangle the dynamic trajectory of ET stress, (b) investigate the potential

115 driving mechanisms of ESI, and (c) quantify the time-varying sensitivity of ESI to principal external drivers upon the incorporation of intrinsic memory effects. As a pixel-level and high-frequency analysis, our findings are expected to narrow the knowledge gap in temporal variability of evapotranspiration stress response, enhance our comprehension of the complex water-vegetation-climate interactions, and offer insights into potential improvements for Earth System Models.

2 Materials and Methods

120 ### 2.1 Study Area and Datasets

2.1.1 Study Area

Located in East Asia (73°33′-135°05′E, 3°51′-53°33′N), China encompasses a vast land area of approximately 9.6 million km² and exhibits diverse climate and vegetation types (Fig. 2). Over the past two decades, the mean air temperature in China
125 has risen by 0.24°C d^{-1} (d^{-1} denotes per decade, the same below), surpassing the global average of 0.2°C d^{-1}. Against the backdrop of a warming climate and proactive greening efforts such as the Three-North Shelter Forest Program, the Grain for Green Program, and the Plain Greening Project (Fu et al., 2024a), there has been a notable rise in the regional LAI by 7.66%—equating to 4.21% d^{-1} (p<0.001). This increase leads the world, with forests and cropland constituting the primary greening types at 42% and 32%, respectively (Chen et al., 2019). Nevertheless, there is a worrying trend of surface soil
130 moisture decline at a rate of 0.08% d^{-1}. In the face of substantial terrestrial environmental changes and anthropogenic activities, notable alterations in hydrology, vegetation, and climatic conditions have occurred in China, rendering it a hotspot for examining the interactions among these factors (Bai et al., 2020; Li et al., 2018; Zheng et al., 2022)

2.1.2 Calculation and validation of the ESI

135 We utilize the ratio of actual evapotranspiration (ETa) to potential evapotranspiration (ETp) to calculate the Evapotranspiration Stress Index (ESI). Prior to investigating the dynamic changes of ESI, we compared the representativeness of three mainstream datasets: the Global Land Evaporation Amsterdam Model v3.7a (daily, 0.25°), the Terra Moderate Resolution Imaging Spectroradiometer (MODIS) MOD16A2GF Version 6.1 (8-day, 500 m), and the European Center for Medium-Range Weather Forecasts (ECMWF) ERA5-Land (hourly, 0.1°). The results are subsequently
140 validated against observational data from 26 eddy covariance (EC) stations (Fig. 2,S3), which are sourced from various observation networks (Information regarding EC stations is provided in Table S1 in Supporting Information). Each sites has at least one year of continuous observations and energy balance residuals < 35 W m^{-2} (calculated using Eq. 1). Before calculation, outlier observations are eliminated using a three-standard-deviation method, and observations recorded on rainy days are excluded. Subsequently, data imputation is conducted using the IterativeImputer tool in Python. The latent heat
145 measured at the EC station is converted to ETa (Eq. 2), while ETp is calculated using the traditional Penman-Monteith method (Eq. 3). Then, the ratio derived from these two values from EC station serves as a metric for validating the reanalysis products (Fig. 2c, S3).

$$Residual = R_n - G - LE - H \tag{1}$$

150 where R_n represents net radiation, G denotes soil heat flux, which is zero on a daily scale, LE refers to daily latent heat, and H represents sensible heat flux, with all units expressed in W m^{-2}.

$$ET_a = \frac{LE}{\lambda} \tag{2}$$

In Eq. 2, the unit of ET_a is mm day^{-1}, with the constant value of λ at 0°C taken as 28.94.
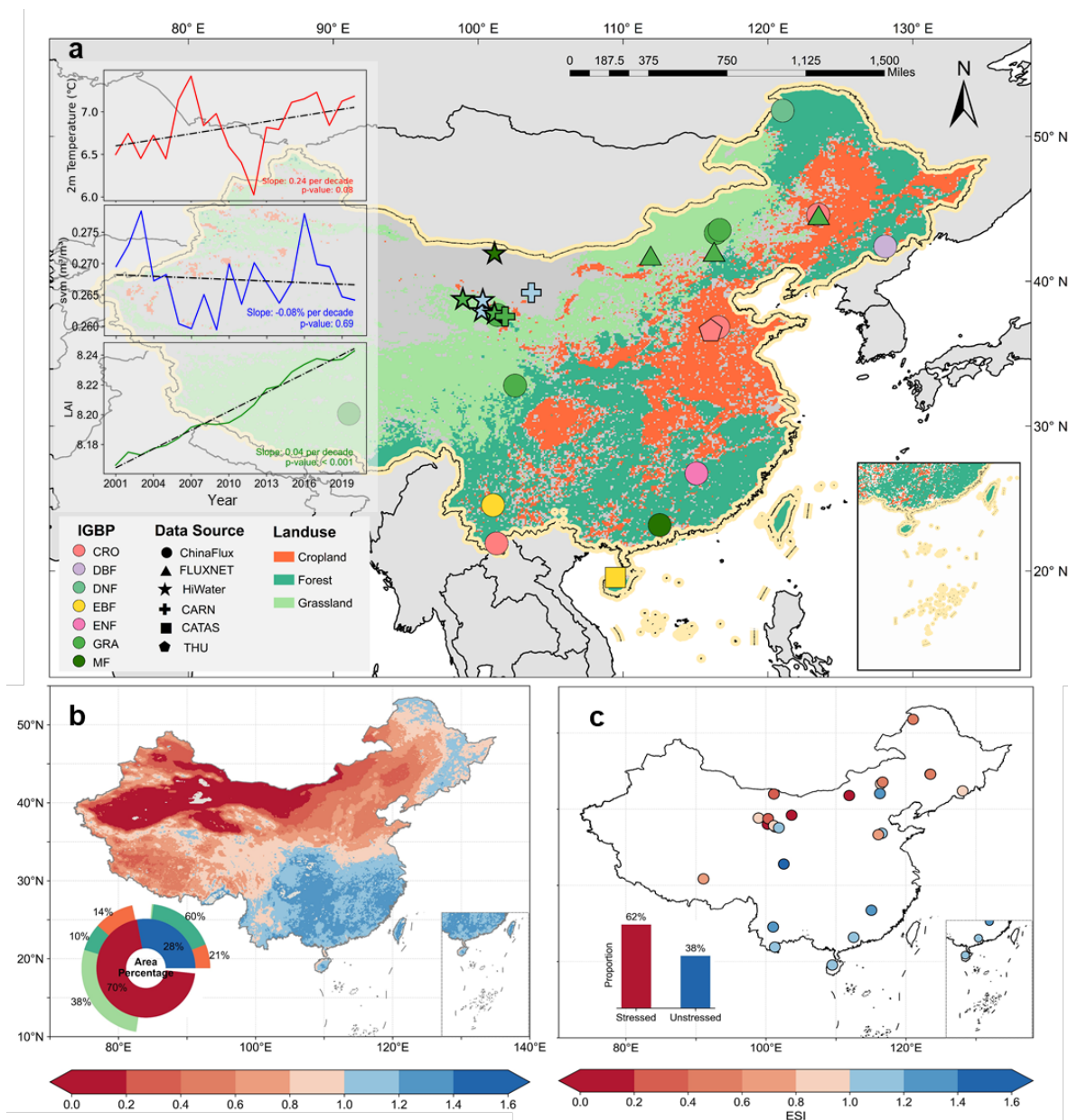
Figure 2. Location of the study area and distribution of multi-year average ESI. (a) The extent of the study area, employing a tri-chromatic map to differentiate between cropland, forest, and grassland; dots denote the positions of EC flux stations, with colors representing the International Geosphere-Biosphere Programme (IGBP) classifications and shapes indicating observational sources. The inset in Panel (a) displays time-series plots of regional average air temperature (red), surface soil moisture (blue), and LAI (green) over the past 20 years, with a black dashed line denoting the linear trend. (b) ESI calculated using ERA5 data (with ETp calculated via the PMCO$_2$ formula). (c) ESI derived from observational data at EC flux stations. Their insets accounted for the proportion of stressed and non-stressed grid areas (equal latitude and longitude projection) or the count of sites, with panel (b) providing a detailed examination of the conditions across various land use types.

165

$$ET_p = \frac{0.408\Delta(R_n - G) + \gamma\frac{900}{T + 273}U(e_s - e_a)}{\Delta + \gamma(1 + 0.34U)} \tag{3}$$

where the unit of ET_p is mm day^{-1}, Δ is the slope of the saturation vapour pressure versus temperature curve (kPa °C^{-1}), γ is the psychrometric constant (kPa °C^{-1}), U is wind speed at 2 m (m s^{-1}), T is surface air temperature (°C), es and ea are saturated and actual vapour pressure (kPa) and whose difference serves as a crucial indicator of atmospheric moisture deficit, known as vapor pressure deficit (VPD). At the grid scale, all climatic variables used to calculate ETp, including Rn, T, and U,

170 are obtained from the ERA5 dataset. In this dataset, VPD is calculated based on the Clausius-Clapeyron relation using 2m temperature and dew point temperature (Held and Soden, 2006; Zhong et al., 2023).

To prevent the overestimation of ETp, we employed the formula developed by Yang et al., (2019) to calculate grid ETp while accounting for the CO_2 water-saving effect (Eq. 4). All meteorological data used in the formula were sourced from ERA5, and the monthly CO_2 data were obtained from CarbonTracker (CT2022) for the period from 2001 to 2020, with a

175 spatial resolution of 3° × 2°. For comparison, after considering the water-saving effect of CO_2, the mean, maximum, and minimum values of ETp in China decreased by 9.48 mm, 30.85 mm, and 19.42 mm, respectively, while the pattern is mirrored (Fig. S1).

$$ET_p = \frac{0.408\Delta(R_n - G) + \gamma\frac{900}{T + 273}U(e_s - e_a)}{\Delta + \gamma\{1 + U[0.34 + 2.4 \times 10^{-4}([CO_2] - 300)]\}} \tag{4}$$

where $2.4 \times 10^{-4}([CO_2] - 300)$ denotes the effect of atmospheric CO_2 concentration (ppm) on surface stomatal resistance

180 (Lian et al., 2021; Zhang et al., 2023).

To compare the effects of CO2 water-saving measures on the ESI, the ERA5 dataset, which is also based on the principles of the Penman-Monteith formula (Eq. 3), was selected for the grid dataset. Its distribution aligns with the patterns observed at EC flux stations (Fig. 2bc, S2). Note that our research is dedicated to analyzing the temporal dynamics of the ESI, particularly in relation to the intensification of drought conditions. The conceptual diagram (Fig. 1) demonstrates that lower

185 ESI values signify increasingly severe imbalances and stress levels. The study does not address how often the threshold of 1 is crossed nor explores the physical significance of this threshold.

2.1.3 Drivers of ESI

In addition to the meteorological and CO_2 data utilized in ETp calculations (Eq. 4), total precipitation (Prec), atmospheric pressure (P), and soil volumetric water content (svm) across different soil layers from ERA5 are also considered as

190 influencing factors for the ESI. To determine the soil moisture within the root zone (0-100 cm) and throughout the entire soil column (0-289 cm), a weighted average method is utilized (Luo et al., 2023). Vegetation factors, which also play a role in driving the ESI, are accounted for using the Global Land Surface Satellite (GLASS) datasets for the Leaf Area Index (LAI) (V60) and Fractional Vegetation Cover (FVC) (V40) (Liang et al., 2013, 2014, 2021), which provide an 8-day temporal resolution and a 0.05° spatial resolution from 2001 to 2020. Moreover, Moderate Resolution Imaging Spectroradiometer

195 (MODIS) datasets, including the Normalized Difference Vegetation Index (NDVI) and Enhanced Vegetation Index (EVI) (MOD13C1) with a 16-day temporal resolution, are applied. Kernel density estimation is utilized to smooth the NDVI data, resulting in a kernel NDVI (kNDVI) that is believed to mitigate saturation effects and enhance robustness to noise (Camps-Valls et al., 2021). (Eq. 5).

$$kNDVI = \tanh(NDVI^2) \tag{5}$$

200 Grids with NDVI value below 0.1 are omitted to exclude areas of barren, rock, sand (i.e. deserts) or snow. Moreover, the Aridity Index (AI), is calculated as multiyear average (2001–2020) by the ratio of annual Prec to ETp using the ERA5 dataset. The lower the AI value, the drier the region, which is used to classify the study area into different hydrometeorological zones: sub-humid ($0.5 \leq AI < 0.65$), semi-arid ($0.2 \leq AI < 0.5$), and arid ($0.05 \leq AI < 0.2$). Regions with an AI exceeding 0.65 are categorized as non-dryland areas (Spinoni et al., 2015). To mitigate the effects of land-use

205 changes, the annual China Land Cover Dataset (Yang and Huang, 2021), featuring a 30-meter grid spacing for the years 2001–2020, are employed. Only plots with consistent land cover types—cropland, forest, or grassland—over the entire study duration were selected for further analysis, as depicted in Fig. 2a.

All variables were interpolated to a spatial resolution of 0.1° to match the ERA5 dataset and were composited over three distinct temporal scales: 8-day, 16-day, and monthly. The selection of datasets was guided by criteria that included high

210 accuracy, fine spatial resolution, and a broad temporal coverage.

2.2 Identification of the key drivers

Regarding hydrothermal conditions and vegetation variables, there are several ways to represent each, with a varying number of proxies. For example, vegetation health can be gauged though multiple indicators such as FVC, LAI, NDVI, and kNDVI. In contrast, the energy conditions considered in this study are limited to T and Rn. A disparity in the number of variables

215 may lead to a bias within the model, favoring certain feature groups and thereby undermining the accuracy of feature importance assessments (Liu et al., 2024). More critically, a high degree of correlation between features—known as multicollinearity—may cause overfitting, where the model becomes excessively tailored to the training data, compromising its ability to generalize. Before model construction, it is essential to identify the principal factors influencing ET stress. Explainable machine learning (SHapley Additive exPlanations) offers an efficacious approach to feature selection (Estécio

220 Marcílio Júnior and Eler, 2020; Li et al., 2022a). We utilize explainable machine learning models, specifically XGBoost and Random Forest (RF) regressors, to assess the relative importance of drivers. SHAP values can indicate the marginal contributions of each predictor, with higher SHAP values denoting greater importance (Lundberg and Lee, 2017). Both XGBoost and RF, as ensemble-based approaches, mitigate overfitting risks and bolster result stability, yet they differ in their suitability for various scenarios, data volume, task complexity, and computational efficiency (Breiman, 2001; Chen and

225 Guestrin, 2016). To optimize the regression model, we use grid search techniques and 5-fold cross-validation for parameter refinement. We execute the optimization process at a regional scale encompassing various vegetation types and hydro-climatic zones instead of on a pixel-by-pixel basis to economize on computational resources. Moreover, we employ partial

dependence plots (PDPs) to elucidate the effects of key drivers on the ESI, illustrating the model's average predictive response to changes in individual drivers, with other variables held constant (Friedman, 2001; Štrumbelj and Kononenko, 2014). PDPs provide a visual depiction of the dynamic interplay between ESI predictions and changes in critical factors. Persistent common trends and analogous seasonal patterns can result in overfitting, thereby concealing the actual causal relationships (Li et al., 2022a) (Fig. 3a). In our SHAP model, we input de-seasonalized and detrended anomalies of each variable. Seasonality is mitigated by subtracting the climatological mean, and long-term trends are eliminated through the application of a locally weighted smoothing filter (LOWESS) with a span of 0.3 (Cleveland, 1979).

2.3 Exploration of the time-varying sensitivity

The sensitivity of evaporative stress to key drivers (identified in Sect. 2.2) in this study is a proxy of the response of the ESI to variations in drivers. Given the presence of self-amplify mechanisms, the previous state of evaporative stress can be represented by a lag-5 autocorrelation model. The mathematical expression for sensitivity is as follows:

$$\delta ESI_t = \theta_{ESI1}\delta ESI_{t-1} \sim \theta_{ESI5}\delta ESI_{t-5} + \theta_{Hydr}\delta Hydr_t + \theta_{Ener}\delta Ener_t + \theta_{Clim}\delta Clim_t + \theta_{Vege}\delta Vege_t + \varepsilon \qquad (6)$$

where $\delta Hydr_t$, $\delta Ener_t$, $\delta Clim_t$ and $\delta Vege_t$ are anomalies in hydrological, energy, climatic, and vegetation conditions, respectively, with subscripts indicating that the anomalies are calculated from the current time(t). The corresponding θ represents the sensitivity of evaporative stress investigated in this study, and ε is the error term. $\theta_{ESI1}\delta ESI_{t-1} \sim \theta_{ESI5}\delta ESI_{t-5}$ denotes the stress states from the previous 1 to 5 stages. Considering the lagging effect, we constructed a memory dynamic linear model based on Bayesian forward filtering (MDLM) to analyze the time-varying sensitivity of ESI. This model draws upon the foundational work of Yanlan Liu, (2019) and Yao Zhang et al., (2021), which primarily examines the vegetation's response to antecedent growth states and prevailing climatic conditions.
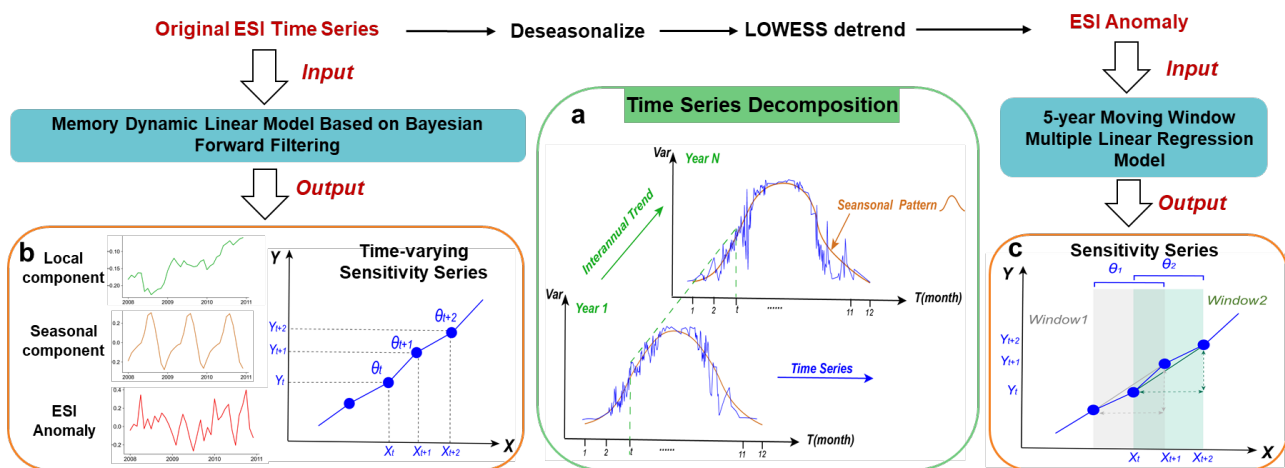

Figure 3. Illustration of time series decomposition and procedures for sensitivity analysis. (a) Conceptual diagram of the time series structure, where the blue line denotes the intra-annual sequence, the green line signifies the interannual trend, and the brown line illustrates the seasonal cycle pattern. (b) The output of the MDLM model. (c) The results from the 5-year moving window multiple linear regression

model, in which Y represents the anomaly of ESI, X denotes the driving factors, θ symbolizes the sensitivity of Y to changes in X, and the subscript denotes the specific time point.

Dynamic linear models serve as a sophisticated statistical methodology for modeling time-series signals by incorporating various contributing factors (Prado et al., 2021). For each pixel, a MLDM was developed, encompassing long-term evaporation stress trends, seasonal cycles, the effects of internal memory from the previous five stages, and various external drivers. DLM effectively decomposes the ESI series into three components: local mean and trend, seasonal pattern, and regression part. The MDLM, utilizing Bayesian forward filtering, enables the prediction of the dynamic relationship between ESI's regression components and driving factors at each timestep, depicting an "instantaneous" response. Additionally, this approach allows sensitivity analysis in both stationary and non-stationary scenarios (Liu, 2019; Zhang et al., 2021b), with model precision increasing as sample size grows. Therefore, we calibrated MLDM using an 8-day resolution, the finest temporal scale available, with data allocation comprising 80% for training and 20% for validation. This split aimed at evaluating the MDLM's accuracy in parameter adjustment and component decomposition of the original ESI series. The training and validation phases demonstrated high and consistent precision, as evidenced by an average R^2, RMSE, and MAE of 0.91, 0.17, and 0.11, respectively (Fig. S10 in Supporting Information), confirming the efficacy of MLDM. Further details on the model are available in Text S1 of the Supporting Information.

Furthermore, we employed a multiple linear regression (MLR) with a 5-year moving window to calculate a rough sensitivity sequence, aiming to verify the accuracy of results from the MDLM. To ensure the sensitivity reflects the relationship between the ESI anomalies and their drivers, we manually subtracted the long-term average within an 8-day interval from the original ESI series to remove seasonality. Subsequently, we applied the LOWESS method to eliminate local trends, thereby obtaining the ESI anomalies. Based on Formula 6, we established a MLR model and analyzed the regression coefficients, namely, the sensitivity coefficients, across each moving window. It is crucial to acknowledge that the sensitivity derived from the MLR model represents an average response across a designated window (Fig. 3c). The MLR provides only an rough sequence of sensitivity, which is utilized to confirm the overarching trend throughout the study period.

The regression coefficients obtained by the two methods are partial regression coefficients, reflecting the magnitude and direction of the relationship between the variable and the ESI while holding other independent variables constant to remove the obfuscating effects of collinearity (Toyoda, 2024). To unveil the intricacies of real-world phenomena more precisely, incorporating a broad spectrum of representative drivers is imperative. To prevent overfitting due to multicollinearity, we evaluated the variance inflation factor (VIF) for the independent variables before modeling (Belsley, 1991) (Table S2 in Supporting Information).

Besides, we employed Sen's slope estimator (Sen, 1968) to quantify the temporal trend and the Mann-Kendall (MK) test to ascertain the statistical significance (Kendall, 1949; Mann, 1945). The slope>0 signifies a positive trend and slope<0 denotes a negative trend over time.

3 Results

285 3.1 Evapotranspiration stress is intensifying in China

China mainland demonstrated a pronounced decline in the ESI from 1950 to 2020 (total change of 4.74%, decreasing by 0.54% d^{-1}, $p < 0.001$). Despite the elevated ESI values accounting for the CO_2 water-saving effect, the downward trend remains largely parallel to the long-term series, indicating a continued exacerbation of evaporative stress (-0.70% d^{-1}, $p = 0.31$). Note that tracking the tendency annually over a 70-year time series confers enhanced statistical significance due to the expanded

290 sample size (Fig. 4a). Collectively, the ESI for each month is on a downward trend. It remains stable during the initial phase of the growing season (0.58±0.08). Commencing in April, the onset of the growing season prompts a marked increase in ESI, coinciding with improved vegetation conditions, and culminates in a peak between 0.9 and 1.0 by August (Fig. 4b). Spatially, over one-quarter (28.01%) of the regions nationwide have registered a significant reduction in ESI ($p < 0.05$), concentrating in the North China Plain and the Northeast where the rate surpassing 2.40% d^{-1}. Concurrently, stress in the Northwest and the

295 middle to lower Yangtze River basin is easing (Fig. 4c). ESI exhibits a sharper decline in dryland (total change of 7.63%, decreasing by 0.91% d^{-1}, $p < 0.001$) compared to the stable and gradual decrease in non-dryland lands (total change of 2.92%, decreasing by 0.32% d^{-1}, $p < 0.01$) (Fig. 4d, S4). This decline is observed universally across various land use categories, with cropland experiencing the most substantial reduction and concurrently exhibiting the highest percentage of areas aggregated (-1.14% d^{-1}, $p < 0.001$; 7.59×10^5 km^2, 50.24% of the total cropland area) (Fig. 4ce, S3, S4). Similar dynamics have been

300 observed in ESI factoring in the water conservation benefits attributed to CO_2. Even so, it is alarming that the decline in ESI for drought-prone and agriculture-intensified regions in the recent two decades has outpaced the rate documented over the preceding 70 years (-1.63% d^{-1} vs -0.91% d^{-1} in dryland, -1.60% d^{-1} vs -1.14% d^{-1} in cropland). Consequently, the progression of water-vegetation-climate stress conditions in these areas necessitates increased scrutiny.
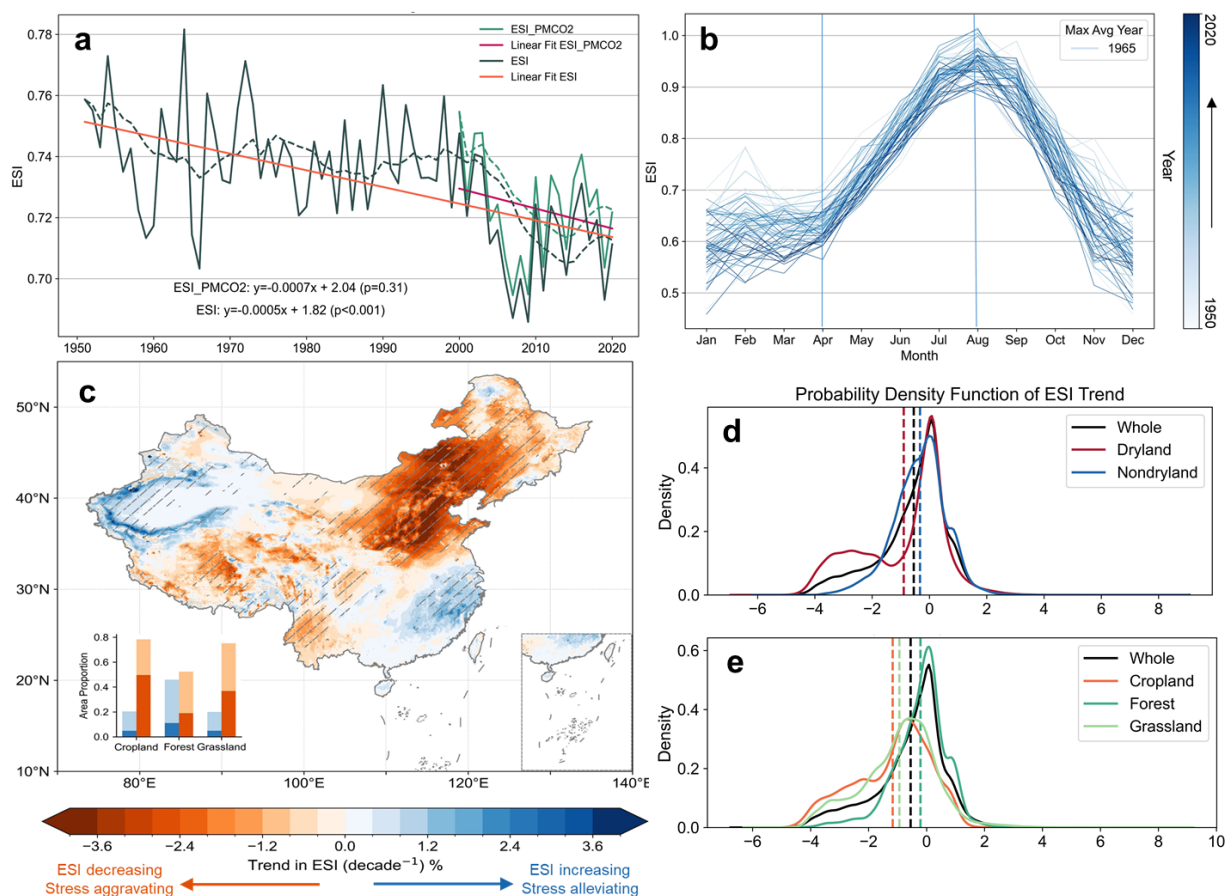
Figure 4. Dynamic trajectory of ESI across China from 1950 to 2020. (a) Time series and linear regression of the mean regional ESI, with the traditional PM equation-derived ESI shown in dark green and the CO_2 water conservation-adjusted ESI in light green. (b) Intra-annual distribution of ESI, with each line corresponding to a different year and darker hues indicating more recent years. (c) ESI trend over the preceding seven decades, quantified by Sen's slope, where lighter shaded regions denote statistically significant trends at the 0.05 level. The inset graphically summarizes the significant (darker shades) and non-significant (lighter shades) changes of ESI across various vegetation types. Panel (d) and (e) illustrate the distribution of ESI trends in both arid and humid zones, as well as across diverse land-use categories.

3.2 Soil moisture as the primary external driver

We assessed the relative importance of water supply, climatic, energy, and vegetation factors on the ESI across various temporal scales and regional characteristics through an interpretable machine learning model utilizing RF regressor. Figure 5 pinpoints shallow soil moisture (0-7cm) as the paramount driver, indicating that its scarcity is most likely to trigger evaporative stress, especially in water-limited regions, consistent with Liebig's law of the minimum. Additionally, an increase in drought severity and a decrease in temporal resolution correspond to a more pronounced augmentation of soil moisture's effect on evaporation (Fig. 5a). Among all the vegetation proxies, LAI performs the best, which is probably attributed to its closest correlation with stomatal conductance (Fig. 5b). Consistent findings were observed when employing the SHAP model that utilizes the XGBoost classifier (Fig. S5). The cross-validation reveals that, across an 8-day interval, the

13

impact of factors associated with water, energy, climate, and vegetation on ESI variability declines sequentially, contributing 44%, 34%, 16%, and 6% to ESI, respectively (Figure 6b). Within each category, the drivers exerting the greatest influence are svm0-7 (0.30), Rn (0.29), VPD (0.10), and LAI (0.02) (Fig. 6a). ESI generally exhibits a nonlinear relationship with

325 several critical factors (Fig. 6c-j). Notably, ESI reduces considerably with a higher VPD, T, Rn, but increases with U, LAI and svm0-7. Moreover, the non-monotonic interactions between P and CO_2 with ESI highlight the imperative for detailed investigation into how these factors influence the exacerbation or mitigation of evaporative stress across various numerical ranges. Interestingly, we observe that the response of ESI to vegetation presents a "plateau-plus-slope" pattern, suggesting that effective mitigation of ET stress occurs only when vegetation cover surpasses a specific threshold (Fig. 6i). Remarkably,

330 when soil moisture anomalies are exceptionally low (ranging from -0.015 to -0.01), there is a sharpened mitigation response, as presented by a near-vertical segment on Fig. 6j. Similar patterns are observed across analyses at various temporal resolutions, reinforcing the robustness of our findings (Fig. S6, S7).
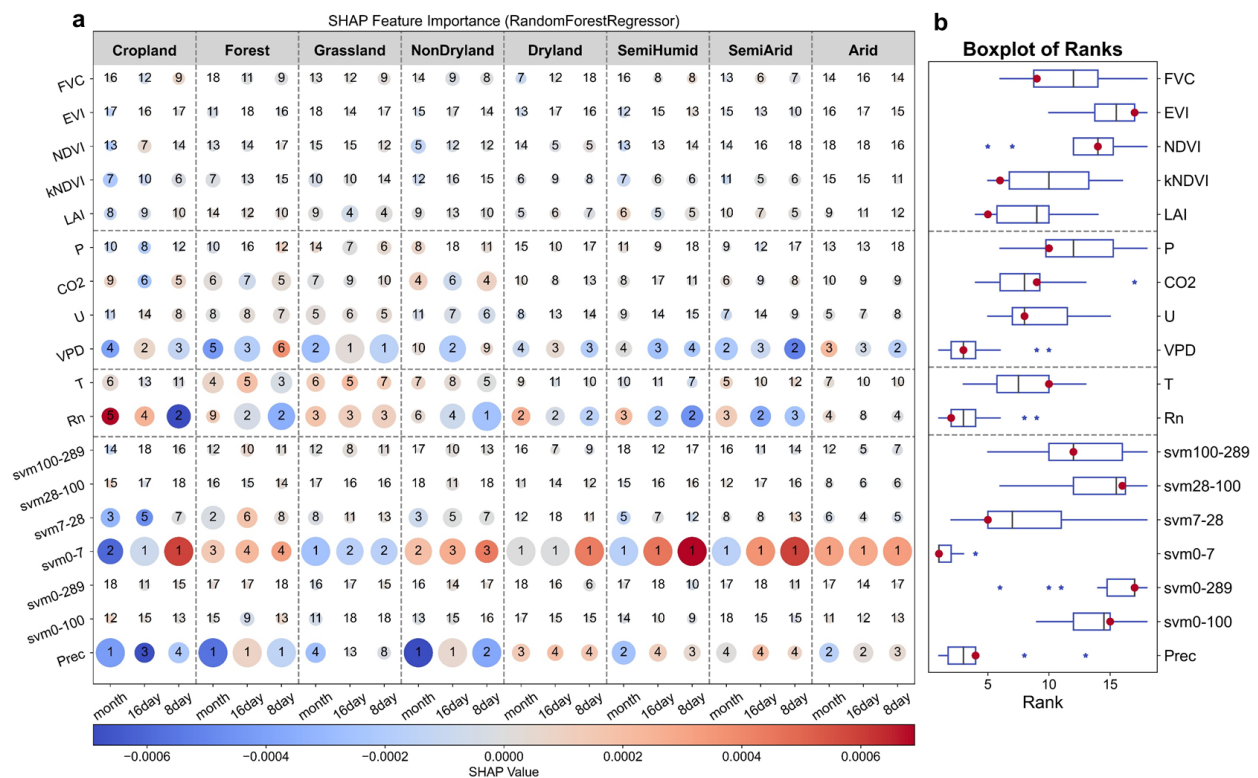

Figure 5. Identification of the key external drivers of evapotranspiration stress index (ESI). (a) Matrix plot employs bubble size to
335 represent the absolute values of SHAP, with a color gradient from blue to red denoting negative and positive effects, respectively. Numerical annotations within each bubble denote the rank of importance for the variables, with higher values signifying greater influence. These ranks are obtained from an explainable machine learning utilizing RF regressors. (b) Boxplot provides a statistical representation of the variable rankings across varying underlying surface conditions (corresponding to the row it's in), where the black line denotes the mean ranking and the red dot signifies the median ranking. The analysis incorporates vegetation factors such as FVC, EVI,
340 NDVI, kNDVI, and LAI; meteorological factors including atmospheric pressure (P), carbon dioxide (CO_2) concentration, wind speed (U), and VPD; energy factors encompass air temperature (T) and net radiation (Rn); and water supply factors, which account for precipitation

(Prec) and the soil volumetric water content (svm) across various soil layer depths, with subscripts specifying the depth range, with 0-7 indicating the soil layer from 0 to 7cm. Inputs to the model are the anomalies of all aforementioned variables.
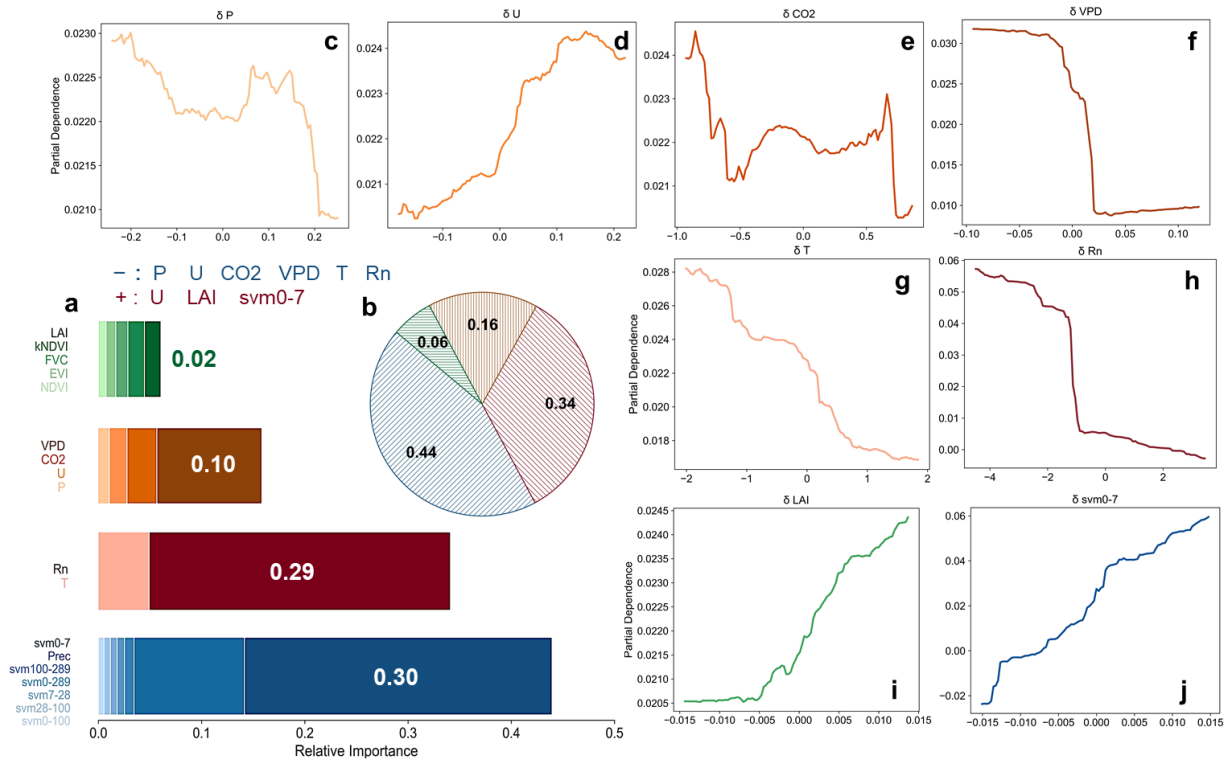
Figure 6. Importance and partial dependence of external driving factors influencing ESI. (a) Relative importance of hydrologic, energy, climatic, and vegetation factors in explaining ESI, with each category encompassing multiple indicators. The significance of these indicators is visually encoded by the color scheme of the bars matching their labels on the left. (b) Pie chart illustrates the proportion of the four categories described in (a). (c-j) Partial dependence graphs correspond to the following variables, in order: P, U, CO_2 concentration, VPD, T, Rn, LAI, and soil moisture content for the top 0-7 cm. This figure is based on an 8-day data series and generated through a SHAP model employing a RF regressors, which processes the anomalies of the variables as inputs.

3.3 Undergoing dramatic changes in sensitivity of key drivers

Our above analysis pinpointed svm0-7, Rn, T, VPD, U, P, CO_2, and LAI as pivotal external drivers of evaporative stress. To quantify the influence of these variables on the ESI, denoted by sensitivity parameter θ (Table S3), factorial simulations are conducted using the MDLM model. The findings demonstrate solid stability and powerful interpretability after successfully passing the multicollinearity test (Table S2). Soil moisture stands out as the paramount and most sensitive factor, with a 1m³ m⁻³ increase in svm0-7 correlating to an estimated 1.49 reduction in ET stress, while the sensitivity of other factors is 2~4 orders of magnitude lower. In the last 20 years, soil moisture sensitivity (θ_{svm}) has demonstrated a marked increase (total change of 8.15%, increasing by 0.11±0.32 d⁻¹, p < 0.001, Fig. 7bc), reaching its peak in 2016 with values 1.48 ~1.76-fold

15

greater than the stable levels of the previous decade. It is paralleled by corresponding results in precipitation as input and corroborated by the MLR method (Fig. S9, S11). Speculatively, it's attributable to the extreme weather conditions of 2016 in China, characterized by flooding in the south and droughts in the north (Yu et al., 2023; Zheng et al., 2024). This climatic anomaly disrupts the historical balance, leading to the atypical variation and pronounced sensitivity peak. Among other

365   pivotal drivers, θ_{VPD} and θ_{LAI} exhibit notable numerical values and considerable trends (Fig. 7, S9). On average, a 1 kPa rise in VPD correlates with an estimated 4.43% (±6.88%) increase in evaporative stress. Conversely, a per-unit increase in LAI can mitigate this stress by approximately 0.52% (±1.46%). As land surface becomes greener and the atmosphere drier(Chen et al., 2019; Yuan et al., 2019), θ_{LAI} markedly diminishes (total change of 0.56%, decreasing by 0.41±2.45% d^{-1}, p < 0.001), while θ_{VPD} progressively escalates (total change of 0.95%, increasing by 0.42±1.75% d^{-1}, p < 0.001, Fig. 7, S9, S11, S12).

370   Contrastingly, the θ_{CO2} shows marked anomalous fluctuations, whereas the role of other factors remained minimal or made virtually no change over time (Fig. S8, S9). Precipitation input scenario and MLR outputs consistently validate these findings. The substantial standard deviations observed above indicate a heterogeneity among various grids in China.

Spatially, sizeable areas (5.89×10^6 km^2, approximately 61-62% of China mainland) experienced a rise of θ_{svm} (Slope >0, Fig. 8a), and no statistically significant differences between dry and wet regions (1.43 vs 1.60, Fig. 8b). Nevertheless, it

375   varies considerably across different land-use types. Forest shows the strongest sensitivity and the most drastic changes, followed by cropland (Fig. 8bc, S13bc). A plausible explanation is that regions endowed with optimal water conditions and robust ecological structure exhibit increased sensitivity due to the magnified impacts resulting from disturbances to the equilibrium of hydrology, climate, and vegetation (Forzieri et al., 2022). Notably, these highly sensitive hotpots distributed near the "Hu Line" and in the lower Yangtze River basin (Fig. 8a). Given the recent shifts in forest composition (large-scale

380   planting of single tree species) coupled with the increasing frequency of extreme climatic events in these areas (Ruan et al., 2022; Yin et al., 2022), special attention is needed. θ_{VPD}, however, exhibits notable regional disparities, with dryland encountering a 3.15-fold greater increase in ET stress per unit of VPD compared to wet regions (θ_{VPD}= 7.91% vs 2.51%). Moreover, θ_{VPD} in arid regions is decreasing (-0.08% d^{-1}, p < 0.01), in contrast to an increasing trend observed in humid regions (0.75% d^{-1}, p < 0.001), so that the discrepancy between dryland and nondryland is anticipated to widen (Fig. 8def,

385   S13def). Consensus results obtained by the MLR method substantiate the authenticity and reliability of the finding (Fig. S13). Interestingly, the response of evaporative stress to LAI (θ_{LAI}) can manifest in both positive and negative ways. Approximately 30% of the national territory (2.87 ×10^6 km^2), counterintuitively, experienced an increase in LAI coupled with intensified ET stress (θ_{LAI} < 0), predominantly in the lower Yangtze River region (Fig. 8g). Regions where increased LAI led to alleviated stress are largely situated in proximity to the "Hu Line" (θ_{LAI} >0, 4.96×10^6 km^2, ~52%). Here, the trend

390   of sensitivity shows a significant decrease (<-0.05 d^{-1}, p < 0.001, Fig. 8h, S13h). Furthermore, this area represents a hotspot for China's afforestation efforts (Zhan et al., 2023), implying that the benefits of sustained greening in reducing ET stress might be lessening. Additionally, the regulation of artificial agronomic measures render minimal and stable θ_{LAI} in cropland (θ_{LAI} = 0.27%, slope = -0.27% d^{-1}, p < 0.01, Fig. 8ij). In contrast, sensitivity comparisons across other land types lack

consistency when derived from two distinct methodologies (Fig. 8ij, S13ij). Consequently, research into the vegetation

395   response within the moisture-climate-vegetation equilibrium should account for temporal scale variations.
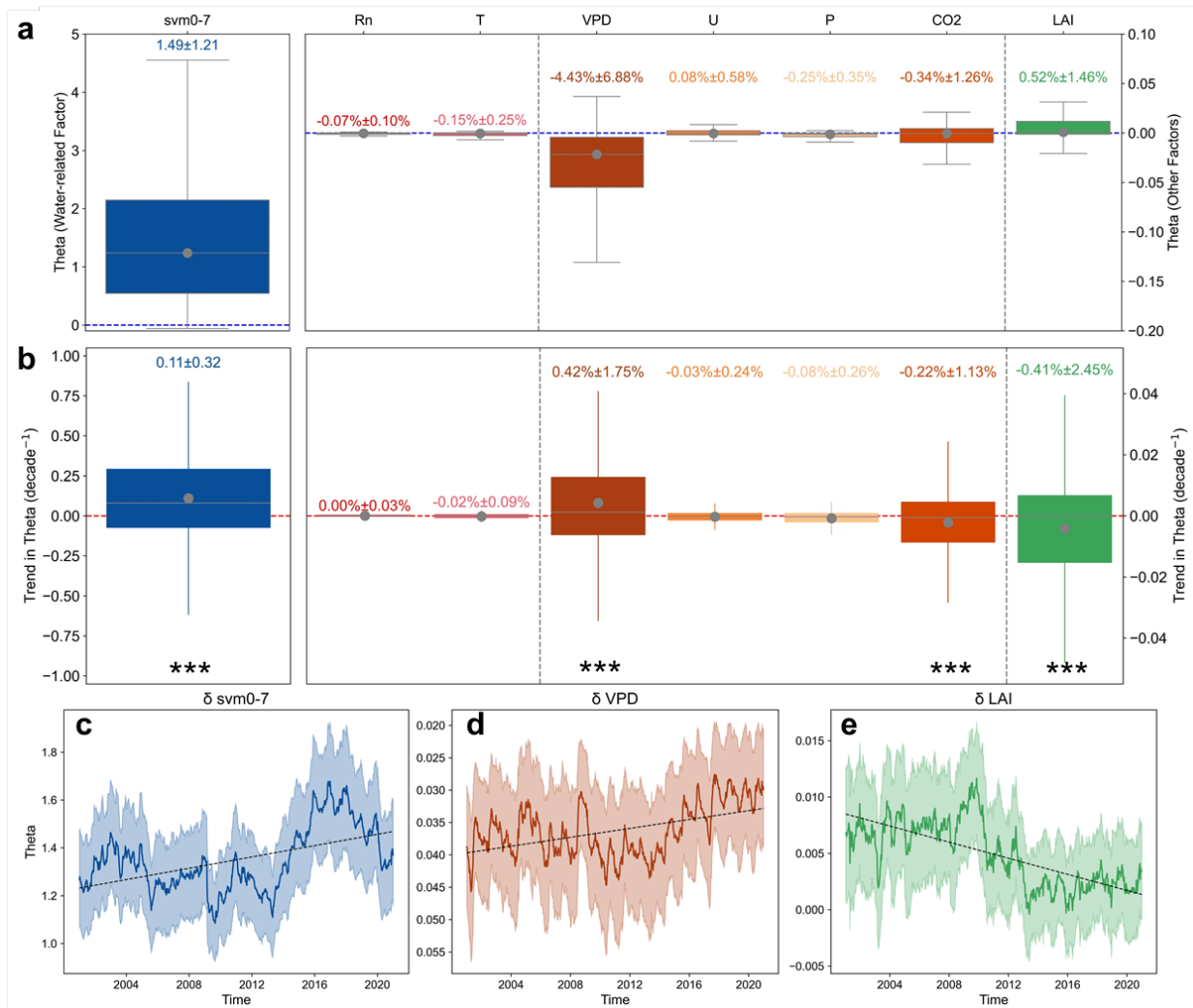
Figure 7. Sensitivity of the ESI to pivotal external drivers and its dynamic sensitivity trajectory. (a) and (b) Box plot of the multi-year mean sensitivity and its changing trend, respectively. In panel (b), the Sen's slope estimator is employed to determine trends, with

400   asterisks denoting statistical significance at a $p < 0.001$. The whiskers and boxes in the box plot denote the range from the maximum to the minimum values, excluding outliers outside the 5% and 95% percentiles, with the upper and lower quartiles represented by the boxes. The median is depicted by a gray line, and the mean by a gray dot, with accompanying text annotations indicating the mean ± standard deviation. (c-e) Series for θ_{svm}, θ_{VPD}, and θ_{LAI}, with shaded regions indicating the standard deviation and a black linear fit line depicting the trend direction. This sensitivity series is calculated from the MLDM, which considers ESI lags from 1 to 5 and incorporates

405   external drivers such as svm0-7, Rn, T, VPD, U, atmospheric CO_2 concentration, and LAI (Parameter Set: R0).
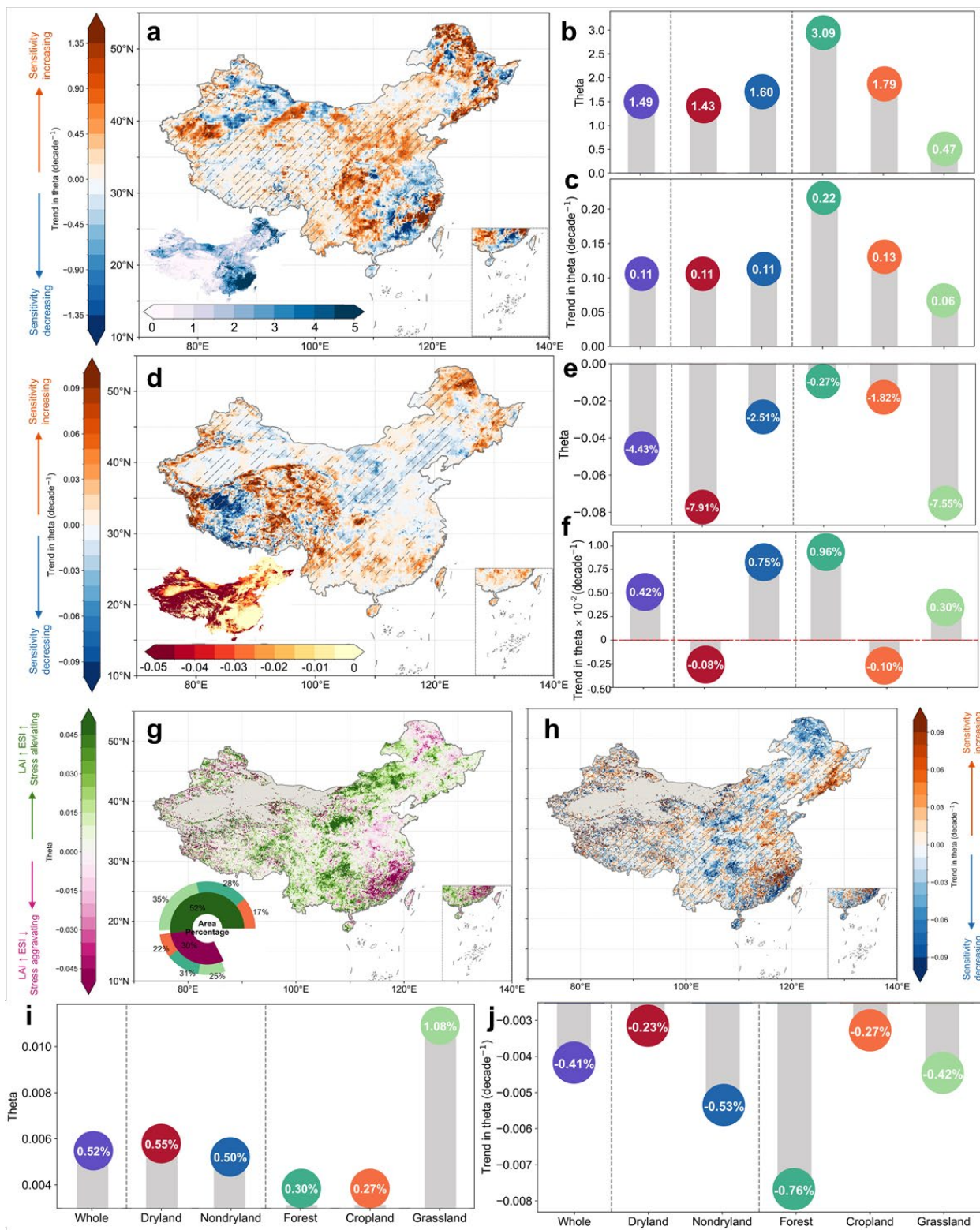
Figure 8. Spatiotemporal heterogeneity in sensitivity of ESI to svm0-7, VPD, and LAI. (a)
Spatial distribution of the trend in $\boldsymbol{\theta_{svm}}$ (sensitivity of ESI to soil water), accompanied by an inset depicting the spatial distribution of
multi-year-average $\boldsymbol{\theta_{svm}}$. (b) and (c) provide the sub-regional statistics for $\boldsymbol{\theta_{svm}}$ and its corresponding trend as shown in (a). (d-f) mirror
(a-c) but for $\boldsymbol{\theta_{VPD}}$. (g) Pattern of $\boldsymbol{\theta_{LAI}}$, with an inset revealing the area statistics categorized by type; within the first ring layer, green
denotes areas where LAI positively influences ESI, while purple signifies areas of negative influence. The second ring layer illustrates the
respective areas of cropland (orange), forest (dark green), and grassland (light green). (i) The sub-regional statistics for $\boldsymbol{\theta_{LAI}}$ as indicated
in figure (g). (h) The distribution of the $\boldsymbol{\theta_{LAI}}$ trend, akin to (a) and (d), with trends estimated by Sen's slope estimator; shaded areas denote
regions where the trend is statistically significant at the 0.05 level through the Mann-Kendall test. (j) The sub-regional statistics for (h).
The sensitivity sequence was derived using the MDLM model configured by the R0 parameter group.

3.4 Sensitivity of soil moisture increases with enhanced greening

In light of the prominent greening tendency in China, we further explored the connection between greening and the
sensitivity of variables that change dramatically (Fig. 9). In extremely humid regions (AI>1.5), areas exhibiting more rapid
greening trends are associated with lower θ_{svm} values (Fig. 9a). Conversely, in less humid regions (AI < 1.5), particularly in
semi-arid and semi-humid areas (0.2 < AI < 0.65), there is a consistent increase in both θ_{svm} and its trend alongside the
gradient of greening trends, suggesting higher sensitivity and greater acceleration (Fig. 9ab). Specifically, when 1.0 <AI<1.5,
θ_{svm} exhibits a progressive increase from 1.64 to 2.78, while the associated trend simultaneously escalates from
approximately 0 to 0.2. In contrast, θ_{VPD} and θ_{LAI} and their trends do not exhibit a co-varying gradient pattern along the
greening trends (Fig. 9d-i). Remarkably, drier regions with slower pace of greening display greater absolute values of θ_{VPD}
($|\theta_{VPD}|$, Fig. 9d), suggesting that heightened VPD amplifies the impact of ET stress on a per-unit basis. However, in areas
with rapid greening, $|\theta_{VPD}|$ tends to be diminished (Fig. 9d), as the enhanced transpiration associated with denser vegetation
could elevate atmospheric moisture levels, potentially offsetting the stress from increased atmospheric moisture deficits(Fig.
9d,f). These findings imply that vegetation greening may, to some extent, enhance the ecosystem's resilience to atmospheric
drought. In humid regions, the band between VPD and ETa or ETp decouple due to surplus water (θ_{VPD}>0, Fig. 9d).
Concerning θ_{LAI}, a higher rate of increase in LAI corresponds to a more rapid decline in θ_{LAI}, resulting in a reduced efficacy
of LAI in mitigating evapotranspiration pressure (Fig. 9h,i). Consequently, the alleviation of water stress achieved through
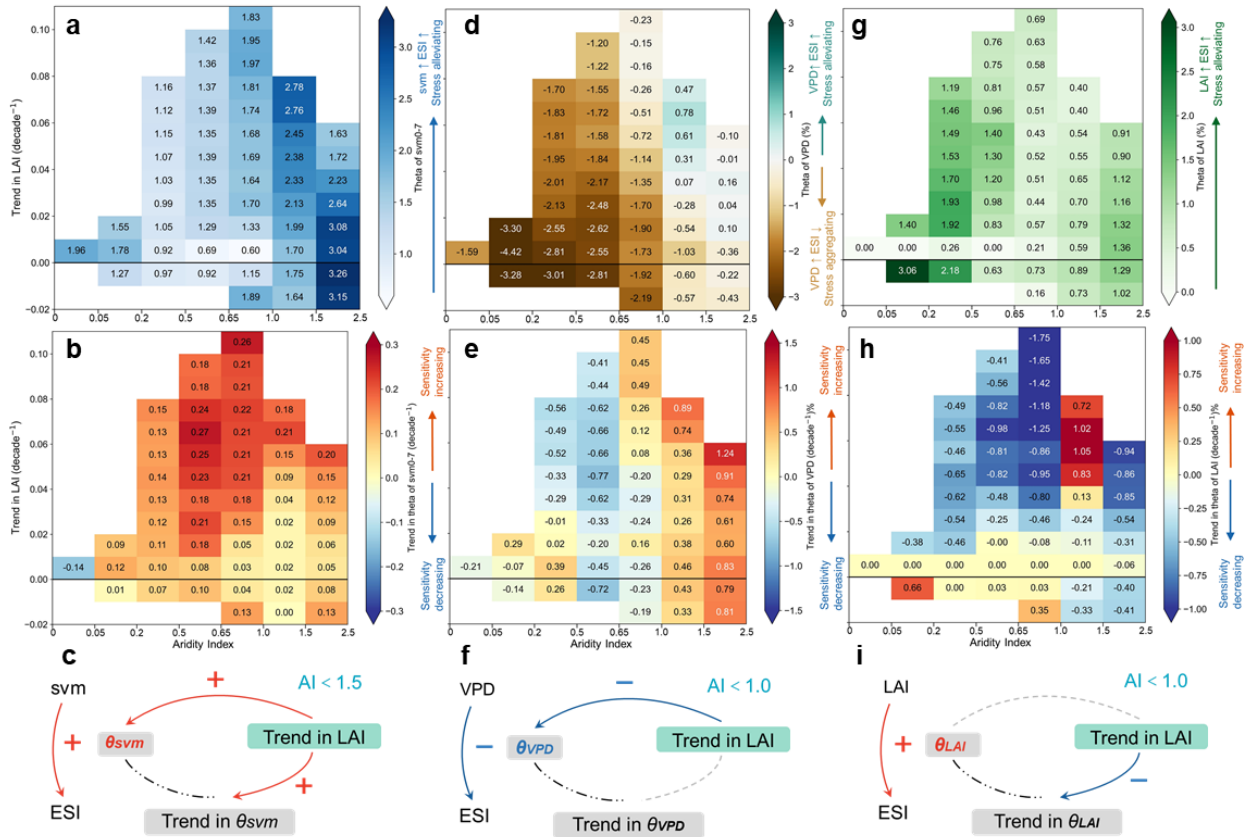greening initiatives might not be as substantial as anticipated.

19

Figure 9. Sensitivity and its trend of ESI to svm0-7, VPD, and LAI along greening and aridity gradient. (a) The grouping statistics of θ_{svm} (sensitivity of ESI to soil water) across different bins, categorized by differing degrees of aridity and trends in LAI. Median value is shown for each grid and the number of grid points within each bin is shown in Supplementary Fig. S15. Similar to (a), (b) pertains to the grouping statistics of the trends of θ_{svm}. (c) The conceptual diagram delineates the covariation between LAI trends and θ_{svm}, including their respective trends, in regions with an Aridity Index (AI) below 1.5. It offers a conceptual interpretation of the patterns depicted in (a) and (b) for these areas. Note that an increase in ESI indicates a mitigation of evaporative stress. Figures (d-f) and (g-h) are analogous to (a-c); however, their protagonist is VPD and LAI, respectively. In figures (c-j), the upper right corner indicates the aridity of regions adhering to the specified pattern. A red line with a "+" sign denotes direct proportionality, whereas a "-" sign accompanied by a blue line indicates inverse proportionality. A grey dashed line represents an ambiguous relationship, and a black dashed line highlights the sensitivity parameter θ and its corresponding trend.

4 Discussion and Conclusions

Previous research has largely focused on the long-term average response of individual variables in the hydrological-climatic-vegetation nexus. Our study employs the Evapotranspiration Stress Index (ESI) as a metric to assess the dynamic equilibrium of the system and introduce the MDLM model to capture its time-varying response (Fig. 1). Our findings indicate that despite the water-saving benefits attributed to elevated atmospheric CO_2 levels, various regions across China have distinctly encountered a heightened evaporative stress (Fig. 4ab, S4). This phenomenon is in concordance with several detrimental environmental shifts recently documented, including the desiccation of land surfaces, intensification of evaporation demand,

and depletion of groundwater reserves (Jasechko et al., 2024; Qing et al., 2023; Yuan et al., 2019). The pronounced increase

455 in ET stress in dryland and cropland underscores the vulnerability of these ecosystems (Fig. 4cde, S3, S4ac). This is primarily attributed to the considerable desiccation of soil moisture (Fig. S14a), which serves as the exclusive direct water-supply source for terrestrial evaporation processes—whether through evaporation of land surface or transpiration via plant stomata—and thus exerts a paramount role (Smith and Boers, 2023; Zhao et al., 2023)(Fig. 5-7, S5-S7). In the past 20 years, due to increased soil water sensitivity, soil water variability has led to greater ET stress intensification (Fig. 6j, S6j, S7j).

460 Sporadic studies on time-varying sensitivity also reveal that water supply has a gradually increasing impact on ecosystems (Hu et al., 2023; Li et al., 2022a; Zeng et al., 2022; Zhang et al., 2022). Our simulation scenarios using precipitation as a proxy for moisture also corroborated these findings (Fig. S9bc, S12a). Hence, addressing the threats posed by soil moisture deficits to water and food security in arid cropland becomes imperative when implementing agricultural practices. Notably, despite a relatively moderate increase in forest ET stress (Fig. 4cde, S3, S4e), soil moisture sensitivity emerges both highly

465 pronounced and rapidly enhanced in recent years (Fig. S8bc, S13bc). In regions with favorable hydrological conditions and stable ecological structures, the collapse of the hydrological-climatic-vegetation system can precipitate profoundly adverse effects (Forzieri et al., 2022). Furthermore, in the face of increasingly intense and severe extreme climatic events, complex ecosystems require enhanced scrutiny to formulate proactive strategies.

Additionally, the greening pace may alter the ability of ecosystems against multiple types of water stress. On the one hand,

470 in semi-arid and -humid regions, the sensitivity of ESI to soil moisture and its variability are proportional to the greening trend (Fig. 9abc). Therefore, once a soil drought occurs, the adverse impact on ET stress increases, suggesting that overly rapid greening can diminish an ecosystem's resilience to soil drought. Specifically, when afforestation surpasses the carrying capacity dictated by regional hydroclimatic conditions, a slight soil deficit can trigger the self-amplify cycle and result in the degradation and mortality of vegetation, known as overshoot drought (Zhang et al., 2021b). From a long-term lens, the

475 reliance on irrigation in the initial stages of artificial vegetation establishment, aimed at ensuring plant survival, can hamper the formation of deep root systems (Moreno-Mateos et al., 2020; Xiao et al., 2024b). Such a practice undermines the plant-groundwater linkage in dryland, subsequently diminishing their resilience (Wang et al., 2023). On the other hand, VPD sensitivity and the greening trend exhibit an inverse gradient (Fig. 9d), indicating that greening has improved the ability to cope with atmospheric drought. This harmonizes well with many statistics and modeling studies(Cui et al., 2022; Zhang et

480 al., 2024). Concerning LAI, a more rapid greening trend correlates with a diminishing contribution of LAI growth to the alleviation of water stress (Fig. 9d, 8h, S13h). Furthermore, in certain regions, an enhanced LAI may exacerbate water stress (Fig. 8g). Gleason et al., (2017) has found that high vegetation density may exacerbate inter-species competition for water, leading to increased water stress for individual plants or specific plant communities, providing a cogent explanation for our outcome. Collectively, although greening has traditionally been considered a positive environmental adjustment, we

485 advocate for a more critical and dialectical understanding. In adherence to sustainable development imperatives, policymakers and decision-makers are tasked with the precise identification of regions amenable to greening initiatives and the establishment of quantifiable benchmarks that will safeguard ecological equilibrium and foster enduring sustainability.

The MDLM model we have developed stands out for its mechanism-focused design and user-friendly operation. It circumvents the prerequisite of anomaly pre-extraction attributable to trends and seasonality by specific parameter configurations. Furthermore, the relatively low average decision coefficients ($R^2 < 0.65$, Fig. S11, S12) derived from the conventional moving window multivariate linear regression method suggest that variable interrelationships within a time block are do not adhere to a strictly linear pattern. Fortuitously, the MDLM adeptly approximates nonlinear processes as quasi-linear physical phenomena at discrete temporal junctures(Liu, 2019; Zhang et al., 2022) (Fig. 3). Note that, however, our study is subject to certain limitations. Firstly, the observational sample size from flux stations is insufficient, as it has been employed solely for the screening of reanalysis products rather than for dynamic factorial simulations. Secondly, the substantial standard deviations observed in some groups indicate that other local factors, such as soil texture, vegetation acclimation, plant demographic rates, and vegetation-groundwater dependency, may exert considerable influence (Abel et al., 2024; Fu et al., 2024b; Patel et al., 2021). More in-depth studies based on long-term ecophysiological observations and purpose-built field experiments are required to further unravel the complex mechanisms of VPD, soil moisture, and LAI in land-atmosphere interactions.

Finally, what are the key implications given the foreglimpse of intensifying evapotranspiration stress driven by the increasing sensitivity to soil water deficits in a greening China? Soil water variability would lead to greater changes in the ecosystems undergoing rapid greening. That is, stronger drought effects can be expected when soil water is anomalously low. Concurrently, the increase in LAI may not alleviate evaporative stress as much as expected. Combined with the increasing frequency and severity of extreme climate events, a "greening but drying" trend may thus be more prevalent in the future, potentially raising the risk of ecosystem imbalance. Our work fills a critical gap in our understanding of the spatiotemporal variation in relationship between variables. It can not only facilitate the refinement of conventionally static parameters in Earth System Models but also steer ongoing greening-related strategies towards a more stable equilibrium among water, atmosphere, and vegetation.

Data Availability Statement. Detailed sources of observations from 26 Eddy Covariance Flux Towers are shown in Table S1 in Supporting Information. The Global Land Evaporation Amsterdam Model v3.7a can be downloaded from the GLEAM home/landing page (https://www.gleam.eu/). The Terra Moderate Resolution Imaging Spectroradiometer (MODIS) MOD16A2GF Version 6.1 is accessed from https://lpdaac.usgs.gov/products/mod16a2gfv061/. Meteorological variables are available from The European Center for Medium-Range Weather Forecasts (ECMWF) ERA5-Land (https://cds.climate.copernicus.eu/cdsapp#!/dataset/reanalysis-era5-land?tab=overview). The monthly CO_2 data were obtained from CarbonTracker (CT2022) (https://gml.noaa.gov/ccgg/carbontracker/download.php). LAI (V60) and FVC (V40) from the Global Land Surface Satellite (GLASS) datasets are obtained from http://www.glass.umd.edu/Download.html. NDVI and EVI in version MOD13C1 are derived from https://lpdaac.usgs.gov/products/mod13c1v061/. The annual China Land Cover Dataset with a resolution of 30 meters originates from https://zenodo.org/records/8176941.

References

535 Abel, C., Maestre, F. T., Berdugo, M., Tagesson, T., Abdi, A. M., Horion, S., and Fensholt, R.: Vegetation resistance to increasing aridity when crossing thresholds depends on local environmental conditions in global drylands, Commun Earth Environ, 5, 379, https://doi.org/10.1038/s43247-024-01546-w, 2024.

Allen, R. G., Pereira, L. S., Raes, D., and Smith, M.: Crop evapotranspiration : guidelines for computing crop water requirements, 1998.

540 Anderson, M. C., Hain, C., Otkin, J., Zhan, X., Mo, K., Svoboda, M., Wardlow, B., and Pimstein, A.: An Intercomparison of Drought Indicators Based on Thermal Remote Sensing and NLDAS-2 Simulations with U.S. Drought Monitor Classifications, Journal of Hydrometeorology, 14, 1035–1056, https://doi.org/10.1175/JHM-D-12-0140.1, 2013.

Anderson, M. C., Zolin, C. A., Sentelhas, P. C., Hain, C. R., Semmens, K., Tugrul Yilmaz, M., Gao, F., Otkin, J. A., and Tetrault, R.: The Evaporative Stress Index as an indicator of agricultural drought in Brazil: An assessment based on crop
545 yield impacts, Remote Sensing of Environment, 174, 82–99, https://doi.org/10.1016/j.rse.2015.11.034, 2016.

Bai, P., Liu, X., Zhang, Y., and Liu, C.: Assessing the Impacts of Vegetation Greenness Change on Evapotranspiration and Water Yield in China, Water Resources Research, 56, e2019WR027019, https://doi.org/10.1029/2019WR027019, 2020.

Belsley, D. A.: A Guide to using the collinearity diagnostics, Computer Science in Economics and Management, 4, 33–50, https://doi.org/10.1007/BF00426854, 1991.

550 Breiman, L.: Random Forests, Machine Learning, 45, 5–32, https://doi.org/10.1023/A:1010933404324, 2001.

Camps-Valls, G., Campos-Taberner, M., Moreno-Martínez, Á., Walther, S., Duveiller, G., Cescatti, A., Mahecha, M. D., Muñoz-Marí, J., García-Haro, F. J., Guanter, L., Jung, M., Gamon, J. A., Reichstein, M., and Running, S. W.: A unified vegetation index for quantifying the terrestrial biosphere, Sci. Adv., 7, eabc7447, https://doi.org/10.1126/sciadv.abc7447, 2021.

555   Chen, C., Park, T., Wang, X., Piao, S., Xu, B., Chaturvedi, R. K., Fuchs, R., Brovkin, V., Ciais, P., Fensholt, R., Tømmervik, H., Bala, G., Zhu, Z., Nemani, R. R., and Myneni, R. B.: China and India lead in greening of the world through land-use management, Nat Sustain, 2, 122–129, https://doi.org/10.1038/s41893-019-0220-7, 2019.

Chen, T. and Guestrin, C.: XGBoost: A Scalable Tree Boosting System, Proceedings of the 22nd ACM SIGKDD International Conference on Knowledge Discovery and Data Mining, https://doi.org/10.1145/2939672.2939785, 2016.

560   Cleveland, W. S.: Robust Locally Weighted Regression and Smoothing Scatterplots, Journal of the American Statistical Association, 74, 829–836, https://doi.org/10.1080/01621459.1979.10481038, 1979.

Cui, J., Lian, X., Huntingford, C., Gimeno, L., Wang, T., Ding, J., He, M., Xu, H., Chen, A., Gentine, P., and Piao, S.: Global water availability boosted by vegetation-driven changes in atmospheric moisture transport, Nat. Geosci., 15, 982–988, https://doi.org/10.1038/s41561-022-01061-7, 2022.

565   De Jong, R., Verbesselt, J., Zeileis, A., and Schaepman, M.: Shifts in Global Vegetation Activity Trends, Remote Sensing, 5, 1117–1133, https://doi.org/10.3390/rs5031117, 2013.

Dong, J., Dirmeyer, P. A., Lei, F., Anderson, M. C., Holmes, T. R. H., Hain, C., and Crow, W. T.: Soil Evaporation Stress Determines Soil Moisture-Evapotranspiration Coupling Strength in Land Surface Modeling, Geophysical Research Letters, 47, e2020GL090391, https://doi.org/10.1029/2020GL090391, 2020.

570   Estécio Marcílio Júnior, W. and Eler, D.: From explanations to feature selection: assessing SHAP values as feature selection mechanism, https://doi.org/10.1109/SIBGRAPI51738.2020.00053, 2020.

Feng, S., Liu, J., Zhang, Q., Zhang, Y., Singh, V. P., Gu, X., and Sun, P.: A global quantitation of factors affecting evapotranspiration variability, Journal of Hydrology, 584, 124688, https://doi.org/10.1016/j.jhydrol.2020.124688, 2020.

Forzieri, G., Dakos, V., McDowell, N. G., Ramdane, A., and Cescatti, A.: Emerging signals of declining forest resilience
575   under climate change, Nature, 608, 534–539, https://doi.org/10.1038/s41586-022-04959-9, 2022.

Friedman, J. H.: Greedy function approximation: A gradient boosting machine., Ann. Statist., 29, https://doi.org/10.1214/aos/1013203451, 2001.

Fu, F., Wang, S., Wu, X., Wei, F., Chen, P., and Grünzweig, J. M.: Locating Hydrologically Unsustainable Areas for Supporting Ecological Restoration in China's Drylands, Earth's Future, 12, e2023EF004216,
580   https://doi.org/10.1029/2023EF004216, 2024a.

Fu, Z., Ciais, P., Feldman, A. F., Gentine, P., Makowski, D., Prentice, I. C., Stoy, P. C., Bastos, A., and Wigneron, J.-P.: Critical soil moisture thresholds of plant water stress in terrestrial ecosystems, Sci. Adv., 8, eabq7827, https://doi.org/10.1126/sciadv.abq7827, 2022.

Fu, Z., Ciais, P., Wigneron, J.-P., Gentine, P., Feldman, A. F., Makowski, D., Viovy, N., Kemanian, A. R., Goll, D. S., Stoy,
585   P. C., Prentice, I. C., Yakir, D., Liu, L., Ma, H., Li, X., Huang, Y., Yu, K., Zhu, P., Li, X., Zhu, Z., Lian, J., and Smith, W. K.: Global critical soil moisture thresholds of plant water stress, Nat Commun, 15, 4826, https://doi.org/10.1038/s41467-024-49244-7, 2024b.

Gentine, P., Green, J. K., Guérin, M., Humphrey, V., Seneviratne, S. I., Zhang, Y., and Zhou, S.: Coupling between the terrestrial carbon and water cycles—a review, Environ. Res. Lett., 14, 083003, https://doi.org/10.1088/1748-9326/ab22d6,
590   2019.

Gleason, K. E., Bradford, J. B., Bottero, A., D'Amato, A. W., Fraver, S., Palik, B. J., Battaglia, M. A., Iverson, L., Kenefic, L., and Kern, C. C.: Competition amplifies drought stress in forests across broad climatic and compositional gradients, Ecosphere, 8, e01849, https://doi.org/10.1002/ecs2.1849, 2017.

Grossiord, C., Buckley, T. N., Cernusak, L. A., Novick, K. A., Poulter, B., Siegwolf, R. T. W., Sperry, J. S., and McDowell, N. G.: Plant responses to rising vapor pressure deficit, New Phytologist, 226, 1550–1566, https://doi.org/10.1111/nph.16485, 2020.

Held, I. M. and Soden, B. J.: Robust Responses of the Hydrological Cycle to Global Warming, Journal of Climate, 19, 5686–5699, https://doi.org/10.1175/JCLI3990.1, 2006.

Hsu, H. and Dirmeyer, P. A.: Soil moisture-evaporation coupling shifts into new gears under increasing CO2, Nat Commun, 14, 1162, https://doi.org/10.1038/s41467-023-36794-5, 2023.

Hu, Y., Wei, F., Fu, B., Zhang, W., and Sun, C.: Ecosystems in China have become more sensitive to changes in water demand since 2001, Commun Earth Environ, 4, 444, https://doi.org/10.1038/s43247-023-01105-9, 2023.

Jasechko, S., Seybold, H., Perrone, D., Fan, Y., Shamsudduha, M., Taylor, R. G., Fallatah, O., and Kirchner, J. W.: Rapid groundwater decline and some cases of recovery in aquifers globally, Nature, 625, 715–721, https://doi.org/10.1038/s41586-023-06879-8, 2024.

Joshi, J., Stocker, B. D., Hofhansl, F., Zhou, S., Dieckmann, U., and Prentice, I. C.: Towards a unified theory of plant photosynthesis and hydraulics, Nat. Plants, 8, 1304–1316, https://doi.org/10.1038/s41477-022-01244-5, 2022.

Jung, M., Reichstein, M., Ciais, P., Seneviratne, S. I., Sheffield, J., Goulden, M. L., Bonan, G., Cescatti, A., Chen, J., De Jeu, R., Dolman, A. J., Eugster, W., Gerten, D., Gianelle, D., Gobron, N., Heinke, J., Kimball, J., Law, B. E., Montagnani, L., Mu, Q., Mueller, B., Oleson, K., Papale, D., Richardson, A. D., Roupsard, O., Running, S., Tomelleri, E., Viovy, N., Weber, U., Williams, C., Wood, E., Zaehle, S., and Zhang, K.: Recent decline in the global land evapotranspiration trend due to limited moisture supply, Nature, 467, 951–954, https://doi.org/10.1038/nature09396, 2010.

Kendall, M. G.: Rank Correlation Methods, 1949.

Kono, Y., Ishida, A., Saiki, S.-T., Yoshimura, K., Dannoura, M., Yazaki, K., Kimura, F., Yoshimura, J., and Aikawa, S.: Initial hydraulic failure followed by late-stage carbon starvation leads to drought-induced death in the tree Trema orientalis, Commun Biol, 2, 8, https://doi.org/10.1038/s42003-018-0256-7, 2019.

Kusch, E., Davy, R., and Seddon, A. W. R.: Vegetation-memory effects and their association with vegetation resilience in global drylands, Journal of Ecology, 110, 1561–1574, https://doi.org/10.1111/1365-2745.13891, 2022.

Li, F., Xiao, J., Chen, J., Ballantyne, A., Jin, K., Li, B., Abraha, M., and John, R.: Global water use efficiency saturation due to increased vapor pressure deficit, Science, 381, 672–677, https://doi.org/10.1126/science.adf5041, 2023.

Li, W., Migliavacca, M., Forkel, M., Denissen, J. M. C., Reichstein, M., Yang, H., Duveiller, G., Weber, U., and Orth, R.: Widespread increasing vegetation sensitivity to soil moisture, Nat Commun, 13, 3959, https://doi.org/10.1038/s41467-022-31667-9, 2022a.

Li, Y., Piao, S., Li, L. Z. X., Chen, A., Wang, X., Ciais, P., Huang, L., Lian, X., Peng, S., Zeng, Z., Wang, K., and Zhou, L.: Divergent hydrological response to large-scale afforestation and vegetation greening in China, Sci. Adv., 4, eaar4182, https://doi.org/10.1126/sciadv.aar4182, 2018.

Li, Y., Qin, Y., and Rong, P.: Evolution of potential evapotranspiration and its sensitivity to climate change based on the Thornthwaite, Hargreaves, and Penman–Monteith equation in environmental sensitive areas of China, Atmospheric Research, 273, 106178, https://doi.org/10.1016/j.atmosres.2022.106178, 2022b.

630 Lian, X., Piao, S., Chen, A., Huntingford, C., Fu, B., Li, L. Z. X., Huang, J., Sheffield, J., Berg, A. M., Keenan, T. F., McVicar, T. R., Wada, Y., Wang, X., Wang, T., Yang, Y., and Roderick, M. L.: Multifaceted characteristics of dryland aridity changes in a warming world, Nat Rev Earth Environ, 2, 232–250, https://doi.org/10.1038/s43017-021-00144-0, 2021.

Liang, S., Zhao, X., Liu, S., Yuan, W., Cheng, X., Xiao, Z., Zhang, X., Liu, Q., Cheng, J., Tang, H., Qu, Y., Bo, Y., Qu, Y., Ren, H., Yu, K., and Townshend, J.: A long-term Global LAnd Surface Satellite (GLASS) data-set for environmental studies,
635 International Journal of Digital Earth, 6, 5–33, https://doi.org/10.1080/17538947.2013.805262, 2013.

Liang, S., Zhang, X., Xiao, Z., Cheng, J., Liu, Q., and Zhao, X.: Global LAnd Surface Satellite (GLASS) Products: Algorithms, Validation and Analysis, Global LAnd Surface Satellite (GLASS) Products, 2014.

Liang, S., Cheng, J., Jia, K., Jiang, B., Liu, Q., Xiao, Z., Yao, Y., Yuan, W., Zhang, X., Zhao, X., and Zhou, J.: The Global Land Surface Satellite (GLASS) Product Suite, Bulletin of the American Meteorological Society, 102, E323–E337,
640 https://doi.org/10.1175/BAMS-D-18-0341.1, 2021.

Liu, L., Zhang, Y., Wu, S., Li, S., and Qin, D.: Water memory effects and their impacts on global vegetation productivity and resilience, Sci Rep, 8, 2962, https://doi.org/10.1038/s41598-018-21339-4, 2018.

Liu, L., Gudmundsson, L., Hauser, M., Qin, D., Li, S., and Seneviratne, S. I.: Soil moisture dominates dryness stress on ecosystem production globally, Nat Commun, 11, 4892, https://doi.org/10.1038/s41467-020-18631-1, 2020a.

645 Liu, Q., Peng, C., Schneider, R., Cyr, D., Liu, Z., Zhou, X., Du, M., Li, P., Jiang, Z., McDowell, N. G., and Kneeshaw, D.: Vegetation browning: global drivers, impacts, and feedbacks, Trends in Plant Science, 28, 1014–1032, https://doi.org/10.1016/j.tplants.2023.03.024, 2023.

Liu, X., Feng, Y., Hu, T., Luo, Y., Zhao, X., Wu, J., Maeda, E. E., Ju, W., Liu, L., Guo, Q., and Su, Y.: Enhancing ecosystem productivity and stability with increasing canopy structural complexity in global forests, Sci. Adv., 10, eadl1947,
650 https://doi.org/10.1126/sciadv.adl1947, 2024.

Liu, Y.: Reduced resilience as an early warning signal of forest mortality, Nature Climate Change, 9, https://doi.org/10.1038/s41558-019-0583-9, 2019.

Liu, Y., Parolari, A. J., Kumar, M., Huang, C.-W., Katul, G. G., and Porporato, A.: Increasing atmospheric humidity and CO_2 concentration alleviate forest mortality risk, Proc. Natl. Acad. Sci. U.S.A., 114, 9918–9923,
655 https://doi.org/10.1073/pnas.1704811114, 2017.

Liu, Y., Kumar, M., Katul, G. G., Feng, X., and Konings, A. G.: Plant hydraulics accentuates the effect of atmospheric moisture stress on transpiration, Nat. Clim. Chang., 10, 691–695, https://doi.org/10.1038/s41558-020-0781-5, 2020b.

Liu, Y., Jiang, Q., Wang, Q., Jin, Y., Yue, Q., Yu, J., Zheng, Y., Jiang, W., and Yao, X.: The divergence between potential and actual evapotranspiration: An insight from climate, water, and vegetation change, Science of The Total Environment,
660 807, 150648, https://doi.org/10.1016/j.scitotenv.2021.150648, 2022.

Liu, Z., Cheng, L., Zhou, G., Chen, X., Lin, K., Zhang, W., Chen, X., and Zhou, P.: Global Response of Evapotranspiration Ratio to Climate Conditions and Watershed Characteristics in a Changing Environment, JGR Atmospheres, 125, e2020JD032371, https://doi.org/10.1029/2020JD032371, 2020c.

Lundberg, S. M. and Lee, S.-I.: A unified approach to interpreting model predictions, in: Proceedings of the 31st
665 International Conference on Neural Information Processing Systems, Red Hook, NY, USA, event-place: Long Beach, California, USA, 4768–4777, 2017.

Luo, X., Li, S., Yang, W., Liu, L., Shi, Y., Lai, Y., Yu, P., Yang, Z., Luo, K., Zhou, T., Yang, X., Wang, X., Chen, S., and Tang, X.: Spatio-temporal changes in global root zone soil moisture from 1981 to 2017, Journal of Hydrology, 626, 130297, https://doi.org/10.1016/j.jhydrol.2023.130297, 2023.

670 Mann, H. B.: Nonparametric Tests Against Trend, Econometrica, 13, 245, 1945.

Mantova, M., Herbette, S., Cochard, H., and Torres-Ruiz, J. M.: Hydraulic failure and tree mortality: from correlation to causation, Trends in Plant Science, 27, 335–345, https://doi.org/10.1016/j.tplants.2021.10.003, 2022.

Moreno-Mateos, D., Alberdi, A., Morriën, E., Van Der Putten, W. H., Rodríguez-Uña, A., and Montoya, D.: The long-term restoration of ecosystem complexity, Nat Ecol Evol, 4, 676–685, https://doi.org/10.1038/s41559-020-1154-1, 2020.

675 Nguyen, H., Wheeler, M. C., Otkin, J. A., Cowan, T., Frost, A., and Stone, R.: Using the evaporative stress index to monitor flash drought in Australia, Environ. Res. Lett., 14, 064016, https://doi.org/10.1088/1748-9326/ab2103, 2019.

Otkin, J. A., Zhong, Y., Lorenz, D., Anderson, M. C., and Hain, C.: Exploring seasonal and regional relationships between the Evaporative Stress Index and surface weather and soil moisture anomalies across the United States, Hydrol. Earth Syst. Sci., 22, 5373–5386, https://doi.org/10.5194/hess-22-5373-2018, 2018.

680 Patel, K. F., Fansler, S. J., Campbell, T. P., Bond-Lamberty, B., Smith, A. P., RoyChowdhury, T., McCue, L. A., Varga, T., and Bailey, V. L.: Soil texture and environmental conditions influence the biogeochemical responses of soils to drought and flooding, Commun Earth Environ, 2, 127, https://doi.org/10.1038/s43247-021-00198-4, 2021.

Peng, L., Zeng, Z., Wei, Z., Chen, A., Wood, E. F., and Sheffield, J.: Determinants of the ratio of actual to potential evapotranspiration, Global Change Biology, 25, 1326–1343, https://doi.org/10.1111/gcb.14577, 2019.

685 Prado, R., Ferreira, M. A. R., and West, M.: Time Series: Modeling, Computation, and Inference, , https://doi.org/10.1201/9781351259422, 2021.

Qing, Y., Wang, S., Yang, Z.-L., Gentine, P., Zhang, B., and Alexander, J.: Accelerated soil drying linked to increasing evaporative demand in wet regions, npj Clim Atmos Sci, 6, 205, https://doi.org/10.1038/s41612-023-00531-y, 2023.

Richard, Y., Martiny, N., Fauchereau, N., Reason, C., Rouault, M., Vigaud, N., and Tracol, Y.: Interannual memory effects 690 for spring NDVI in semi-arid South Africa, Geophysical Research Letters, 35, 2008GL034119, https://doi.org/10.1029/2008GL034119, 2008.

Ruan, F., Yang, Y., McVicar, T. R., Guo, H., and Hou, Y.: Historical and future shifts of a sharp zonal aridity gradient: A case study of the Hu Line in China, Journal of Hydrology, 614, 128590, https://doi.org/10.1016/j.jhydrol.2022.128590, 2022.

Scheffer, M., Bascompte, J., Brock, W. A., Brovkin, V., Carpenter, S. R., Dakos, V., Held, H., Van Nes, E. H., Rietkerk, M., 695 and Sugihara, G.: Early-warning signals for critical transitions, Nature, 461, 53–59, https://doi.org/10.1038/nature08227, 2009.

Sen, P. K.: Estimates of the Regression Coefficient Based on Kendall's Tau, Journal of the American Statistical Association, 63, 1379–1389, https://doi.org/10.1080/01621459.1968.10480934, 1968.

Seneviratne, S. I., Corti, T., Davin, E. L., Hirschi, M., Jaeger, E. B., Lehner, I., Orlowsky, B., and Teuling, A. J.:
700 Investigating soil moisture–climate interactions in a changing climate: A review, Earth-Science Reviews, 99, 125–161,
https://doi.org/10.1016/j.earscirev.2010.02.004, 2010.

Smith, T. and Boers, N.: Global vegetation resilience linked to water availability and variability, Nat Commun, 14, 498,
https://doi.org/10.1038/s41467-023-36207-7, 2023.

Smith, T., Traxl, D., and Boers, N.: Empirical evidence for recent global shifts in vegetation resilience, Nat. Clim. Chang.,
705 12, 477–484, https://doi.org/10.1038/s41558-022-01352-2, 2022.

Spinoni, J., Vogt, J., Naumann, G., Carrao, H., and Barbosa, P.: Towards identifying areas at climatological risk of
desertification using the Köppen-Geiger classification and FAO aridity index: TOWARDS IDENTIFYING AREAS AT
CLIMATOLOGICAL RISK OF DESERTIFICATION, Int. J. Climatol, 35, 2210–2222, https://doi.org/10.1002/joc.4124,
2015.

710 Štrumbelj, E. and Kononenko, I.: Explaining prediction models and individual predictions with feature contributions,
Knowledge and Information Systems, 41, 647–665, https://doi.org/10.1007/s10115-013-0679-x, 2014.

Sulman, B. N., Roman, D. T., Yi, K., Wang, L., Phillips, R. P., and Novick, K. A.: High atmospheric demand for water can
limit forest carbon uptake and transpiration as severely as dry soil, Geophysical Research Letters, 43, 9686–9695,
https://doi.org/10.1002/2016GL069416, 2016.

715 Thornthwaite, C. W.: An Approach toward a Rational Classification of Climate, Geographical Review, 38, 55,
https://doi.org/10.2307/210739, 1948.

Toyoda, H.: Interpretation of Partial Regression Coefficients, in: Statistics with Posterior Probability and a PHC Curve,
Springer Nature Singapore, Singapore, 261–279, https://doi.org/10.1007/978-981-97-3094-0_16, 2024.

Wang, T., Wu, Z., Wang, P., Wu, T., Zhang, Y., Yin, J., Yu, J., Wang, H., Guan, X., Xu, H., Yan, D., and Yan, D.: Plant-
720 groundwater interactions in drylands: A review of current research and future perspectives, Agricultural and Forest
Meteorology, 341, 109636, https://doi.org/10.1016/j.agrformet.2023.109636, 2023.

Xiao, L., Wu, X., Zhao, S., and Zhou, J.: Memory effects of vegetation after extreme weather events under various
geological conditions in a typical karst watershed in southwestern China, Agricultural and Forest Meteorology, 345, 109840,
https://doi.org/10.1016/j.agrformet.2023.109840, 2024a.

725 Xiao, T., Li, P., Fei, W., and Wang, J.: Effects of vegetation roots on the structure and hydraulic properties of soils: A
perspective review, Science of The Total Environment, 906, 167524, https://doi.org/10.1016/j.scitotenv.2023.167524, 2024b.

Yang, J. and Huang, X.: The 30 m annual land cover dataset and its dynamics in China from 1990 to 2019, Earth Syst. Sci.
Data, 13, 3907–3925, https://doi.org/10.5194/essd-13-3907-2021, 2021.

Yang, Y., Roderick, M. L., Zhang, S., McVicar, T. R., and Donohue, R. J.: Hydrologic implications of vegetation response
730 to elevated CO2 in climate projections, Nature Clim Change, 9, 44–48, https://doi.org/10.1038/s41558-018-0361-0, 2019.

Yin, X., Zhou, L.-T., Liu, K., Han, Y., and Du, Z.: Record-breaking flood over the Yangtze River in early summer 2020: role
of the north Indian Ocean and north tropical Atlantic SST, Theor Appl Climatol, 150, 1173–1186,
https://doi.org/10.1007/s00704-022-04217-y, 2022.

Yu, Y., You, Q., Zuo, Z., Zhang, Y., Cai, Z., Li, W., Jiang, Z., Ullah, S., Tang, X., Zhang, R., Chen, D., Zhai, P., and Shrestha, S.: Compound climate extremes in China: Trends, causes, and projections, Atmospheric Research, 286, 106675, https://doi.org/10.1016/j.atmosres.2023.106675, 2023.

Yuan, W., Zheng, Y., Piao, S., Ciais, P., Lombardozzi, D., Wang, Y., Ryu, Y., Chen, G., Dong, W., Hu, Z., Jain, A. K., Jiang, C., Kato, E., Li, S., Lienert, S., Liu, S., Nabel, J. E. M. S., Qin, Z., Quine, T., Sitch, S., Smith, W. K., Wang, F., Wu, C., Xiao, Z., and Yang, S.: Increased atmospheric vapor pressure deficit reduces global vegetation growth, Sci. Adv., 5, eaax1396, https://doi.org/10.1126/sciadv.aax1396, 2019.

Zeng, X., Hu, Z., Chen, A., Yuan, W., Hou, G., Han, D., Liang, M., Di, K., Cao, R., and Luo, D.: The global decline in the sensitivity of vegetation productivity to precipitation from 2001 to 2018, Global Change Biology, 28, 6823–6833, https://doi.org/10.1111/gcb.16403, 2022.

Zhan, Y., Ma, C., Yan, Y., Zhu, J., Ji, Y., Ma, C., and Luo, Y.: Spatial differentiation characteristics of vegetation greening rates and climate attribution in China's arid and semi-arid regions, Global Ecology and Conservation, 46, e02563, https://doi.org/10.1016/j.gecco.2023.e02563, 2023.

Zhang, J., Guan, K., Peng, B., Pan, M., Zhou, W., Jiang, C., Kimm, H., Franz, T. E., Grant, R. F., Yang, Y., Rudnick, D. R., Heeren, D. M., Suyker, A. E., Bauerle, W. L., and Miner, G. L.: Sustainable irrigation based on co-regulation of soil water supply and atmospheric evaporative demand, Nat Commun, 12, 5549, https://doi.org/10.1038/s41467-021-25254-7, 2021a.

Zhang, Y., Keenan, T. F., and Zhou, S.: Exacerbated drought impacts on global ecosystems due to structural overshoot, Nat Ecol Evol, 5, 1490–1498, https://doi.org/10.1038/s41559-021-01551-8, 2021b.

Zhang, Y., Gentine, P., Luo, X., Lian, X., Liu, Y., Zhou, S., Michalak, A. M., Sun, W., Fisher, J. B., Piao, S., and Keenan, T. F.: Increasing sensitivity of dryland vegetation greenness to precipitation due to rising atmospheric CO_2, Nat Commun, 13, 4875, https://doi.org/10.1038/s41467-022-32631-3, 2022.

Zhang, Y., Zheng, H., Zhang, X., Leung, L. R., Liu, C., Zheng, C., Guo, Y., Chiew, F. H. S., Post, D., Kong, D., Beck, H. E., Li, C., and Blöschl, G.: Future global streamflow declines are probably more severe than previously estimated, Nat Water, https://doi.org/10.1038/s44221-023-00030-7, 2023.

Zhang, Y., Feng, X., Zhou, C., Sun, C., Leng, X., and Fu, B.: Aridity threshold of ecological restoration mitigated atmospheric drought via land–atmosphere coupling in drylands, Commun Earth Environ, 5, 381, https://doi.org/10.1038/s43247-024-01555-9, 2024.

Zhao, D., Zhang, Z., and Zhang, Y.: Soil Moisture Dominates the Forest Productivity Decline During the 2022 China Compound Drought-Heatwave Event, Geophysical Research Letters, 50, e2023GL104539, https://doi.org/10.1029/2023GL104539, 2023.

Zheng, H., Miao, C., Li, X., Kong, D., Gou, J., Wu, J., and Zhang, S.: Effects of Vegetation Changes and Multiple Environmental Factors on Evapotranspiration Across China Over the Past 34 Years, Earth's Future, 10, e2021EF002564, https://doi.org/10.1029/2021EF002564, 2022.

Zheng, T., Zheng, Z., Feng, G., Zhao, Y., and Fan, P.: Characteristics of regional heavy rainfall in the pre-flood season in South China and prediction skill of NCEP S2S, Clim Dyn, https://doi.org/10.1007/s00382-024-07181-7, 2024.

Zhong, Z., He, B., Wang, Y.-P., Chen, H. W., Chen, D., Fu, Y. H., Chen, Y., Guo, L., Deng, Y., Huang, L., Yuan, W., Hao, X., Tang, R., Liu, H., Sun, L., Xie, X., and Zhang, Y.: Disentangling the effects of vapor pressure deficit on northern terrestrial vegetation productivity, SCIENCE ADVANCES, 2023.